A Fast and Accurate Semi-Analytical Solution for Lumped Models of Co-Current Moving Bed Reactors

Sávio L. Bertoli[1†], Jesús Efraín Apolinar-Hernández[1†], Carolina K. de Souza[2], Marcel Jeferson Gonçalves[2], Cíntia Soares[1*], Natan Padoin[1*]

[1]*Laboratory of Materials and Scientific Computing (LabMAC), Chemical and Food Engineering Department, Federal University of Santa Catarina (UFSC), 88040-970, Florianópolis, Santa Catarina, Brazil.*

[2]*Chemical Engineering Department, University of Blumenau (FURB), 89030-000, Blumenau, Santa Catarina, Brazil.*

† These authors contributed equally to the work.

savio.leandro@posgrad.ufsc.br, jesus.hernandez@posgrad.ufsc.br, carolinakrebs@furb.br, marcelg@furb.br, cintia.soares@ufsc.br, natan.padoin@ufsc.br

[*]Corresponding authors.
E-mail addresses: cintia.soares@ufsc.br (C. Soares), natan.padoin@ufsc.br (N. Padoin)

Abstract

Moving bed reactors (MBRs) are widely used in various industrial processes, making the development of mathematical models crucial for their design, optimization, and control. This study presents a semi-analytical solution (SAS) for a lumped parameter kinetic and heat transfer model of a tubular MBR, where a first-order chemical reaction occurs uniformly within the particles. SAS is developed using the concepts of the finite analytic method: decomposition of the problem domain into small intervals, keeping the terms as linear and evaluated under the conditions at the beginning of each interval, and obtaining local analytical solutions in these intervals. SAS is a fast, consistent, and unconditionally stable numerical scheme that can handle very stiff systems ($SR = 10^{305}$). A comparison of the SAS results with those of traditional ODE solvers – explicit Euler, Heun, Ralston, and Runge-Kutta of 3rd, 4th, and 5th order – shows excellent agreement. Moreover, for a case study with Biot number less than 0.11 and fourth Damköhler number less than 1.5, the comparison of SAS with a numerical solution (using the finite difference method) of a distributed parameter model, shows a maximum relative error of 0.17%, 0.04% and 6.3% for particle temperature, fluid temperature and conversion, respectively. SAS is (partially) validated by comparison with experimental data from thermogravimetric analysis of kaolinite calcination. In addition, a specific methodology for error analysis is presented, which allows rounding and linearization errors to be estimated.

Keywords: Heat transfer; Moving bed reactors; Numerical analysis; Numerical solution; Semi-analytical solution; Very stiff systems.

Graphical Abstract

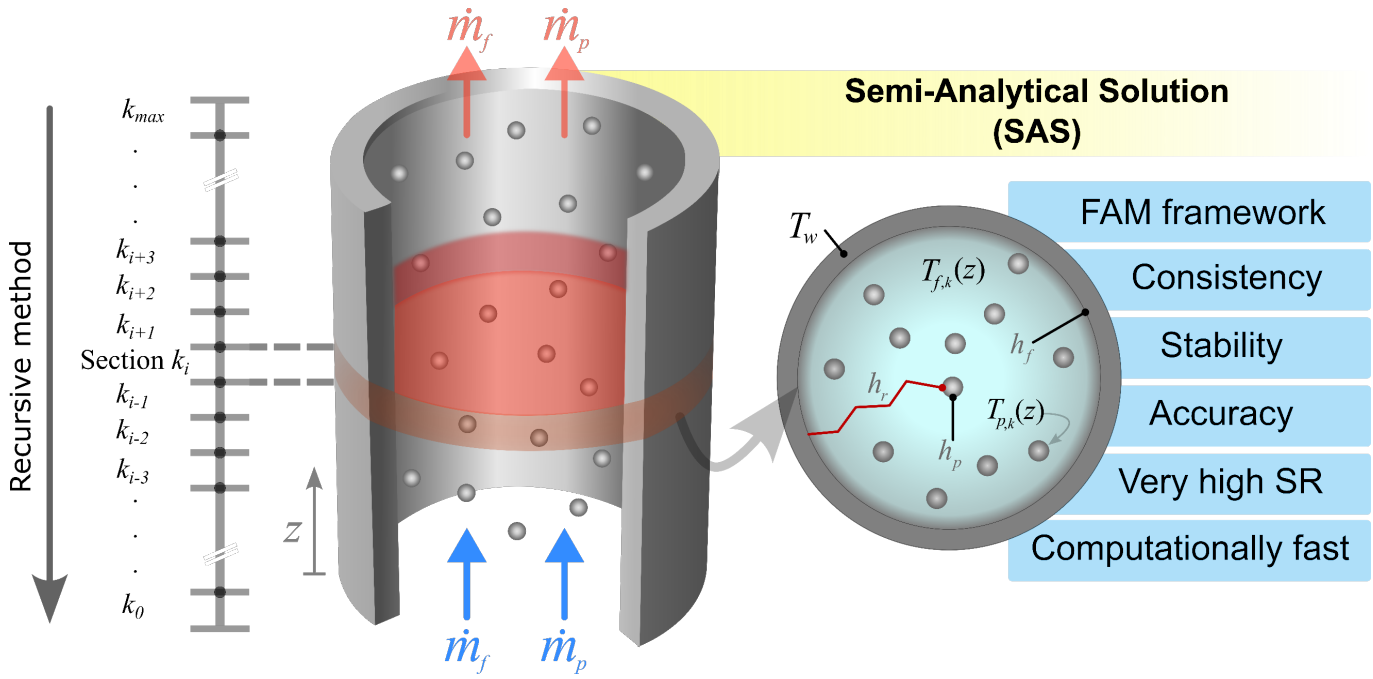

1. Introduction

There are several technological applications for heat and/or mass transfer between solid particles and one or more fluid phases. We can highlight, for example, the pyrolysis of shale oil fines in moving beds (Lisbôa, 1987; Bertoli 1989, 2000), the waste tire pyrolysis in moving and fluidized beds (Aylón et al., 2010; Martinez et al., 2013), the flash kaolinite calcination in moving and fluidized beds (Teklay et al., 2014, 2015, 2016), the Fischer-Tropsch synthesis in fixed-bed reactors (Apolinar-Hernández et al., 2024), as well as others industrial processes described in Shirzad et al. (2019).

However, these applications require high equipment efficiency levels, making it essential to model the phenomena involved for scaling up and process optimization. Therefore, several studies in MBR modeling with analytical and/or numerical solutions have been carried out, such as: Munro and Amundson (1950), Leung and Quon (1965), Lisbôa (1987), Bertoli (1989, 2000), Bertoli and Hackenberg (1990), Fan and Zhu (1998), Saastamoinen (2004), Meier et al. (2009), Almendros-Ibáñez et al. (2011), Bertoli et al. (2012, 2015a, 2015b, 2017, 2019, 2020, 2022, 2023, 2024), Yang et al. (2015), Isaza et al. (2016), Medeiros et al. (2018, 2021), Tribess et al. (2022).

Among these studies, the works of de Almeida Jr. (2016) and Bertoli et al. (2015a) are directly related to this investigation. The authors developed a semi-analytical solution of a lumped parameter model (Walas, 1965; Leung and Quon, 1965) to the butane pyrolysis process, with the assumed conditions: first-order chemical reaction in gas phase, reactor with adiabatic walls, particles considered as spheres and inert. The model solution was developed using the concepts of the Finite-Analytic Method (FAM) (Chen and Li, 1980) with the difference that first, using integrating factors, an integral representation of the model equations is developed; then, by linearization and discretization of the resulting coupled system of integral equations, the interval solution is obtained.

Furthermore, the work of Medeiros et al. (2018, 2021) is also directly related to the study presented herein. The authors developed a semi-analytical solution for an isothermal wall MBR model to distributed parameters in the particles and to lumped parameters in the fluid phase (hereinafter this model and the semi-analytical solution of Medeiros et al. (2018, 2021) will simply be referred to as DM and SA, respectively),

assuming – among other simplifications – irreversible chemical reaction occurring uniformly within spherical particles, and constant radiative heat transfer coefficient h_r – this hypothesis was mitigated by means of a corrective step, in which h_r is taken equal to the arithmetic mean between its value at the reactor inlet and its value at the discretization point. The solution was developed from the analytical solution of the associated homogeneous (linear) problem (Meier et al., 2009) and the spectral expansion of the non-homogeneous vector. The simulations accurately predicted kaolinite flash calcination's temperature and conversion profiles (Teklay et al., 2016). The main distinctions between DM and the model of this study are as follows: in the latter, the particle is modeled to lumped parameters, a strategy that simplifies the model. Regarding the implementation of the solutions, in SAS, h_r is evaluated locally, i.e., at the discretization point, in better correspondence to physical reality. In SA, however, it is assumed to be constant throughout the reactor (or corrected, as described above). Furthermore, although the DM is to distributed parameters for the solid phase, the SA assumes, for each discretization interval, a uniform reaction rate for the particle (calculated at a volumetric average particle temperature).

SAS will be developed using FAM concepts (Chen and Li, 1980): decomposition of the problem region into small intervals; maintaining terms as linear and evaluated under the conditions at the beginning of each interval; obtaining local analytical solutions in these intervals. Although there are studies/applications aiming to generalize the FAM (e.g., Civan, 1995, 2009; de Almeida Jr., 2016; de Almeida Jr. et al., 2016; Lemos et al., 2016), one of the difficulties in applying of the original finite analytical method is since for each case there is a solution. Several applications of the method (see, Chen and Li, 1980) demonstrate this difficulty. Among the applications of FAM for chemically reactive systems is the work of Ardestani et al. (2015), who used the practical FAM proposed by Civan (1995, 2009) to solve a model to describe the transport of contaminants dissolved in groundwater.

2. Mathematical modeling

The heat transfer model of a moving bed reactor was developed based on the mass and energy conservation laws using the single particle approach. Fig. 1 shows schematically a co-current moving bed

reactor and the control volume for which the analysis is performed. The MBR is modelled to lumped parameters to solid particles and lumped parameters to fluid phase. It is considered tubular, vertical and diluted, with each particle surrounded only by the dragging fluid. Inside the particles, a first-order irreversible chemical reaction takes place uniformly. Other assumptions are (Bertoli, 1989, 2000, 2020; Meier et al., 2009; Medeiros et al., 2021): steady state operation, physical and transport properties uniform and constant, spherical particles with a uniform and constant radius and uniformly distributed over the cross-section of the reactor, developed flow, fluid temperature and velocity profiles considered uniform in the cross-section of the reactor (particles and fluid may have different velocities), conveyor fluid transparent to thermal radiation, reactor wall considered as an isothermal blackbody, axial heat dispersion considered negligible in comparison with the advective energy flux, wall-particle radiative heat flux described by a linearized form of the Stefan-Boltzmann equation, negligible interaction effects between particles and particle-wall, and negligible thermal effects due to viscous dissipation or particle friction.

Insert Figure 1

2.1 Governing equations

Considering the previous hypotheses and introducing the dimensionless particle residence time

$$\tau \equiv \frac{3h_p}{\rho_p c_p R_p}\acute{t} = \mathrm{Bi_p Fo'} \qquad (1a, b)$$

the dimensionless temperatures,

$$\theta_f(\tau) \equiv \frac{T_f(t_1\tau) - T_{fi}}{T_{pi}} \qquad (2)$$

$$\theta_p(\tau) \equiv \frac{T_p(t_1\tau) - T_{pi}}{T_{pi}} \qquad (3)$$

the reactant conversion, and the dimensionless heat source term due to a first order irreversible chemical reaction,

$$X(\tau) \equiv \frac{C_{Ai} - C_A(t_1\tau)}{C_{Ai}} \qquad (4)$$

$$g(\tau) \equiv \mathrm{Da}_{\mathrm{dev}}\big(1 - X(\tau)\big) \tag{5}$$

and, finally, the dimensionless groups:

$$\mathrm{P}_{\mathrm{y}}' \equiv \frac{3h_p}{\rho_p c_p R_p K} \tag{6}$$

$$\beta \equiv \frac{\dot{m}_p c_p}{\dot{m}_f c_f} \tag{7}$$

$$\varphi \equiv 1 + \frac{h_r}{h_p} \tag{8}$$

$$\omega \equiv 1 + r_{ws}\frac{h_f}{h_p} \tag{9}$$

Then, considering the differential control volume in Fig. 1, the LPM is

$$\frac{dX(\tau)}{d\tau} = \frac{1-X(\tau)}{\mathrm{Py}'} \tag{10}$$

$$\frac{1}{\beta}\frac{d\theta_f(\tau)}{d\tau} = \theta_p(\tau) - \theta_p(\infty) + \omega\left(\theta_f(\infty) - \theta_f(\tau)\right) \tag{11}$$

$$\frac{d\theta_p(\tau)}{d\tau} = \theta_f(\tau) - \theta_f(\infty) + \varphi\left(\theta_p(\infty) - \theta_p(\tau)\right) + g(\tau) \tag{12}$$

subject to the initial conditions (at the reactor's inlet) presented in Eqs. (13) – (15):

$$X(0) = 0 \tag{13}$$

$$\theta_f(0) = 0 \tag{14}$$

$$\theta_p(0) = 0 \tag{15}$$

In the previous equations,

$$\theta_f(\infty) \equiv \frac{T_w - T_{fi}}{T_{pi}} \tag{16}$$

$$\theta_p(\infty) \equiv \frac{T_w - T_{pi}}{T_{pi}} \tag{17}$$

3. Model solution

3.1 Solution procedure

The development of SAS for the Eqs. (10) - (15), proceeds according to the following steps:

i. The reactor is sectioned into a k_{max} number of intervals.

ii. In the interval k, i.e., $[\tau_{k-1}, \tau_k]$, K and φ are evaluated at temperature $T_p(\tau_{k-1})$, and kept constant (K_{k-1} and φ_{k-1}, respectively), making the model equations linear.

iii. The associated linear problem is solved analytically and locally (i.e., in the interval k).

iv. The local solution is iteratively regressed to the reactor inlet ($k = 0$), thus obtaining the SAS.

v. A representation of the SAS in continuous variables, is obtained through limit operations and the definition of integral.

In the next sections, this methodology will be developed. It should be noted, however, that for the computational implementation of SAS, only the results of step *iii* are required.

Note that this procedure differs from that of Vanti et al. (2008) and Bertoli et al. (2015a), because in these works, given the simplicity of the models studied, the SAS in continuous variables was obtained directly from the model equations – i.e., without the previous steps *i-iv* – through integrating factors.

3.2 Model linearization

Initially, the reactor is sectioned into k_{max} intervals. In the k interval, i. e., $[\tau_{k-1}, \tau_k]$, K and φ are evaluated at the temperature $T_p(\tau_{k-1})$ and made constant. Then, we can write from Eqs. (10)-(12), the following linear system of ordinary differential equations (ODEs):

$$\frac{dX(\tau)}{d\tau} = \frac{1-X(\tau)}{\mathrm{Py}'_{k-1}} \tag{18}$$

$$\frac{1}{\beta}\frac{d\theta_f(\tau)}{d\tau} = \theta_p(\tau) - \theta_p(\infty) + \omega\big(\theta_f(\infty) - \theta_f(\tau)\big) \tag{19}$$

$$\frac{d\theta_p(\tau)}{d\tau} = \theta_f(\tau) - \theta_f(\infty) + \varphi_{k-1}\left(\theta_p(\infty) - \theta_p(\tau)\right) + g_{k-1}(\tau) \tag{20}$$

Where

$$g_{k-1}(\tau) \equiv \mathrm{Da}_{\mathrm{dev,k-1}}\big(1 - X(\tau)\big) \tag{21}$$

Subject to the following conditions at the beginning of the interval:

$$X(\tau_{k-1}) = X_{k-1} \tag{22}$$

$$\theta_f(\tau_{k-1}) = \theta_{f,k-1} \tag{23}$$

$$\theta_p(\tau_{k-1}) = \theta_{p,k-1} \tag{24}$$

3.3 Local (interval) solution of the linearized model

Integrating Eq. (18), and using the boundary condition of Eq. (22), we have

$$X_k(\tau) = 1 - (1 - X_{k-1})e^{-\left(\frac{\tau-\tau_{k-1}}{\mathrm{Py}'_{k-1}}\right)} \tag{25}$$

Thus, substituting Eq. (25) into Eq. (21), the thermal generation rate becomes

$$g_{k-1}(\tau) = \mathrm{Da}_{\mathrm{dev},k-1}(1 - X_{k-1})e^{-\left(\frac{\tau-\tau_{k-1}}{\mathrm{Py}'_{k-1}}\right)} \tag{26}$$

As seen, the approach used causes decoupling of reaction kinetics from energy balances, but not vice versa. Therefore, isolating $\theta_p(\tau)$ in Eq. (19), we have

$$\theta_p(\tau) = \theta_p(\infty) + \frac{1}{\beta}\frac{d\theta_f(\tau)}{d\tau} + \omega\left(\theta_f(\tau) - \theta_f(\infty)\right) \tag{27}$$

Substituting Eq. (27) into Eq. (20), one obtains:

$$\frac{d\theta_p(\tau)}{d\tau} = (\omega\varphi_{k-1} - 1)\left(\theta_f(\infty) - \theta_f(\tau)\right) + g_{k-1}(\tau) - \frac{\varphi_{k-1}}{\beta}\frac{d\theta_f(\tau)}{d\tau} \tag{28}$$

Deriving Eq. (19) with respect to τ and substituting Eq. (28) into the result, then $\theta_p(\tau)$ is decoupled from $\theta_f(\tau)$, according to the following equation

$$\frac{1}{\beta}\frac{d^2\theta_f(\tau)}{d\tau^2} + \left(\omega + \frac{\varphi_{k-1}}{\beta}\right)\frac{d\theta_f(\tau)}{d\tau} + (\omega\varphi_{k-1} - 1)\left(\theta_f(\tau) - \theta_f(\infty)\right) = g_{k-1}(\tau) \tag{29}$$

Now, defining

$$\Theta_f(\tau) \equiv \theta_f(\tau) - \theta_f(\infty) \tag{30}$$

then Eq. (29) is rewritten in the form,

$$\frac{1}{\beta}\frac{d^2\Theta_f(\tau)}{d\tau^2} + \left(\omega + \frac{\varphi_{k-1}}{\beta}\right)\frac{d\Theta_f(\tau)}{d\tau} + (\omega\varphi_{k-1} - 1)\Theta_f = g_{k-1}(\tau) \tag{31}$$

The solution of Eq. (31) (inhomogeneous) can be obtained by the Complementary Function Method, in the form (see, for instance, Butkov, 1973)

$$\Theta_f(\tau) = \Theta_{f(hom)}(\tau) + \Theta_{f(part)}(\tau) \tag{32}$$

Where $\Theta_{f(hom)}$ is the general solution of the associated homogeneous (complementary function) and $\Theta_{f(part)}$ is a particular solution.

The solution of the associated homogenous $\Theta_{f(hom)}$ – a 2nd order ODE with constant coefficients –, is standard (Wylie and Barrett, 1990):

$$\Theta_{f(hom)}(\tau) = b_{1,k-1}e^{-r_{1,k-1}\tau} + b_{2,k-1}e^{-r_{2,k-1}\tau} \tag{33}$$

with characteristic equation with the following roots

$$r_{(1,2),k-1} = \frac{-(\beta\omega+\varphi_{k-1})\pm\sqrt{(\beta\omega-\varphi_{k-1})^2+4\beta}}{2} = \frac{-(\beta\omega+\varphi_{k-1})\pm\sqrt{(\beta\omega+\varphi_{k-1})^2+4\beta(1-\varphi_{k-1})}}{2} \tag{34a-d}$$

The solution $\Theta_{f(part)}$ is obtained by the method of undetermined coefficients (Jenson and Jeffreys, 1963):

$$\Theta_{f(part)}(\tau) = b_{3,k-1}\, e^{r_{3,k-1}\tau} \tag{35}$$

Where

$$r_{3,k-1} = -\frac{1}{\mathrm{Py}'_{k-1}} \tag{36}$$

$$b_{3,k-1}e^{r_{3,k-1}\tau_{k-1}} \equiv b'_{3,k-1} = \frac{\beta\,\mathrm{Da}_{\mathrm{dev},k-1}(1-X_{k-1})}{r^2_{3,k-1}+(\beta\omega+\varphi_{k-1})r_{3,k-1}+\beta\omega\varphi_{k-1}-\beta} \tag{37a, b}$$

Thus, substituting the results of Eqs. (33) and (35) into Eq. (32), the general solution of Eq. (35) is

$$\Theta_f(\tau) = \sum_{l=1}^{3} b_{l,k-1}e^{r_{l,k-1}\tau} \tag{38}$$

That is,

$$\theta_f(\tau) = \theta_f(\infty) + \sum_{l=1}^{3} b_{l,k-1}e^{r_{l,k-1}\tau} \tag{39}$$

Substituting Eq. (39) into Eq. (27), we obtain the local solution for the particle temperature

$$\theta_p(\tau) = \theta_p(\infty) + \sum_{l=1}^{3}\left(\frac{r_{l,k-1}}{\beta}+\omega\right) b_{l,k-1}e^{r_{l,k-1}\tau} \tag{40}$$

The coefficients $b_{1,k-1}$ and $b_{2,k-1}$ are determined from Eqs. (39) and (40), and the conditions Eqs. (23) and (24), as follows:

$$b_{1,k-1}e^{r_{1,k-1}\tau_{k-1}} \equiv b'_{1,k-1} = \frac{b'_{3,k-1}(r_{3,k-1}-r_{2,k-1})+(\beta\omega+r_{2,k-1})\left(\theta_{f,k-1}-\theta_f(\infty)\right)-\beta\left(\theta_{p,k-1}-\theta_p(\infty)\right)}{r_{2,k-1}-r_{1,k}} \tag{41a, b}$$

$$b_{2,k-1}e^{r_{2,k-1}\tau_{k-1}} \equiv b'_{2,k-1} = \frac{b'_{3,k-1}(r_{3,k-1}-r_{1,k-1})+(\beta\omega+r_{1,k-1})\left(\theta_{f,k-1}-\theta_f(\infty)\right)-\beta\left(\theta_{p,k-1}-\theta_p(\infty)\right)}{r_{1,k-1}-r_{2,k-1}} \tag{42a, b}$$

3.4 Difference equations

Difference equations to integrate the system of Eqs. (10)-(15) are obtained from Eqs. (25), (36), (39) and (40), as follows:

$$X_k = 1 - (1 - X_{k-1})e^{r_{3,k-1}(\tau_k - \tau_{k-1})} \tag{43}$$

$$\theta_{f,k} = \theta_{fk-1} + \sum_{l=1}^{3} b_{l,k-1}(e^{r_{l,k-1}\tau_k} - e^{r_{l,k-1}\tau_{k-1}}) \tag{44}$$

$$\theta_{p,k} = \theta_{p,k-1} + \sum_{l=1}^{3} \left(\frac{r_{l,k-1}}{\beta} + \omega\right) b_{l,k-1}(e^{r_{l,k-1}\tau} - e^{r_{l,k-1}\tau_{k-1}}) \tag{45}$$

In the above equations, $(\tau_{k-1} \leq \tau \leq \tau_k)$ and $(1 \leq k \leq k_{max})$.

Eqs. (43)-(45), together with Eqs. (34), (36), (37), (41) and (42), are used to calculate, recursively, the conversion and temperatures along the MBR. Alternatively, and for numerical stability purposes, one can rewrite the above equations as follows:

$$X_k = 1 - (1 - X_{k-1})e^{r_{3,k-1}\Delta\tau} \tag{46}$$

$$\theta_{f,k} = \theta_{f,k-1} + \sum_{l=1}^{3} b'_{l,k-1}\,(e^{r_{l,k-1}\Delta\tau} - 1) \tag{47}$$

$$\theta_{p,k} = \theta_{p,k-1} + \sum_{l=1}^{3} \left(\frac{r_{l,k-1}}{\beta} + \omega\right) b'_{l,k-1}\,(e^{r_{l,k-1}\Delta\tau} - 1) \tag{48}$$

Where $b'_{1,k-1}$, $b'_{2,k-1}$ and $b'_{3,k-1}$, are respectively given by Eqs. (41), (42) and (37), and

$$\Delta\tau = \tau_k - \tau_{k-1} \tag{49}$$

3.5 SAS (recursive solution)

From Eqs. (46)-(48) and using the inlet conditions Eqs. (13)-(15), the SAS is obtained by recursion:

$$X_k = 1 - e^{\Delta\tau \sum_{j=1}^{k} r_{3,j-1}} \tag{50}$$

$$\theta_{f,k} = \sum_{j=1}^{k} \sum_{l=1}^{3} b_{l,j-1}(e^{r_{l,j-1}\tau_j} - e^{r_{l,j-1}\tau_{j-1}}) \tag{51}$$

$$\theta_{p,k} = \sum_{j=1}^{k} \sum_{l=1}^{3} \left(\frac{r_{l,k-1}}{\beta} + \omega\right) b_{l,j-1}(e^{r_{l,j-1}\tau_j} - e^{r_{l,j-1}\tau_{j-1}}) \tag{52}$$

3.6 SAS in continuous variables

A representation of SAS in continuous variables can be obtained from Eqs. (50)-(52) by making $\Delta\tau \to 0$ (i. e. , $k_{max} \to \infty$), summing the series, and using the definition of definite integral. Proceeding in this way, one obtains:

$$X(\tau) = 1 - e^{\int_0^\tau r_3 d\tau} \tag{53}$$

$$\theta_f(\tau) = \sum_{l=1}^{3} \int_0^\tau b_l r_l e^{r_l \tau} d\tau \tag{54}$$

$$\theta_p(\tau) = \sum_{l=1}^{3} \int_0^\tau \left(\frac{r_l}{\beta} + \omega\right) b_l r_l e^{r_l \tau} d\tau \tag{55}$$

Where

$$r_{(1,2)} = \frac{-(\beta\omega+\varphi) \pm \sqrt{(\beta\omega-\varphi)^2+4\beta}}{2} \tag{56a, b}$$

$$r_3 = -\frac{1}{\mathrm{Py}'} \tag{57}$$

$$b_1 = \frac{b_3(r_3-r_2)e^{r_3\tau} + (\beta\omega+r_2)\left(\theta_f(\tau)-\theta_f(\infty)\right) - \beta\left(\theta_p(\tau)-\theta_p(\infty)\right)}{r_2-r_1} e^{-r_1\tau} \tag{58}$$

$$b_2 = \frac{b_3(r_3-r_1)e^{r_3\tau} + (\beta\omega+r_1)\left(\theta_f(\tau)-\theta_f(\infty)\right) - \beta\left(\theta_p(\tau)-\theta_p(\infty)\right)}{r_1-r_2} e^{-r_2\tau} \tag{59}$$

$$b_3 = \frac{\beta \mathrm{Da}_{\mathrm{dev}}\left(1-X(\tau)\right)}{r_3^2+(\beta\omega+\varphi)r_3+\beta\varphi\omega-\beta} e^{-r_3\tau} \tag{60}$$

In Eqs. (53)-(60), the parameters r_l, b_l $(l = 1, 2, 3)$, $\mathrm{Da}_{\mathrm{dev}}$, Py', and φ are now continuous functions of $T_p(\tau)$. Thus, the SAS in continuous variables is expressed by a system of coupled implicit integral equations. In Appendix B, it is shown that SAS in continuous variables satisfies the model equations and, therefore, is an exact representation of the model.

4. Residence time scales

To deepen the physical understanding of the results, the following particle residence time scales (see also Bertoli et al., 2012, 2016, 2017, 2019, 2022; Tribess et al., 2022) are introduced in Table 1.

Insert Table 1

Once these scales are defined, it is interesting to note that:

$$\mathrm{Bi_p} = \frac{t_1}{t_2}, \quad \mathrm{Bi_r} = \frac{t_1}{t_3}, \quad \mathrm{Da_{IV}} = \frac{t_1}{t_6}, \quad \mathrm{Da_{dev}} = \frac{t_2}{t_6}, \quad \mathrm{Fo}' = \frac{t'}{t_1}, \quad \mathrm{Py} = \frac{t_7}{t_1} \tag{61a-l}$$

$$\mathrm{Py}' = \frac{t_7}{t_2}, \quad \mathrm{Th}^2 = \frac{t_1}{t_7}, \quad \beta = \frac{t_2}{t_4}, \qquad \varphi \equiv 1 + \frac{t_2}{t_3}, \quad \tau = \frac{t'}{t_2}, \qquad \omega = 1 + \frac{t_4}{t_5}$$

In addition to enabling a clear physical understanding of the system parameters, scale analysis is also useful in the preliminary model selection. This analysis is postponed to Section 7.4.

5. Case studies

The case studies evaluated by Medeiros et al. (2021) were chosen for analysis carried out herein, for comparison purposes:

a) Heat transfer in a moving bed of oil shale fines (Lisbôa, 1987)

Oil shale fines are a residue from moving bed pyrolysis of oil shale**.** One solution for using these wastes is pyrolysis in co-current MBR (Lisbôa, 1987). In this sense, the heating of a mixture of oil shale fines and air, in a co-current moving bed is selected as case study *a*. Specifically, we will look at Thermal Test (TT) No. 4 of Lisbôa (1987), with the following modifications introduced here: $L = 10$ m, $T_w = 973.15$ K, and a first order reaction in the solid phase is assumed, with the following hypothetical data: $A = 2.0 \times 10^{12}\ \mathrm{s}^{-1}$, $C_{Ai} = 400\ \mathrm{kg/m^3}$, $E = 163.0\ \mathrm{kJ/mol}$, $\Delta H_R = 2534.8\ \mathrm{kJ/kg}$. TT No. 4 of Lisbôa (1987) is also described in Bertoli (2000) and Bertoli et al. (2019).

b) Flash calcination of kaolinite in a moving bed (Teklay et al., 2016)

The flash calcination of kaolin-rich clays is an important aspect in the metakaolin production. The process is carried out in moving bed reactors (Teklay et al., 2015) or fluidized bed reactors (Salvador, 1995), at temperatures between 450 °C and 750 ºC, producing only water vapor (Salvador, 1995; Sperinck et al., 2011; Teklay et al., 2016) and metakaolin, according to the reaction described in Eq. (62) (Bridson et al., 1985; Slade et al., 1992).

$$\mathrm{Al_2Si_2O_5(OH)_4} \xrightarrow{\Delta} \mathrm{Al_2O_3 \,.\, 2\ SiO_2} + 2\ \mathrm{H_2O} \tag{62}$$

In this work, kaolinite calcination kinetics are selected as case study *b*, and will be represented in a simplified way by the kaolinite dehydroxylation step. The conditions, properties and correlations are those used by Teklay et al. (2014) – also described in Medeiros et al (2021). Air is chosen as the dragging fluid.

6. Methodology

6.1 SAS verification and relative performance

The SAS is initially verified by comparison with the linear model solution. case study *a* (Section 5) is used as a benchmark, with the following modifications: h_r and K evaluated at $T_p = 597.2$ K. Thus, nonlinearities are removed from the model. Two discretization levels, $k_{max} = 1$ and $k_{max} = N$, are considered. The discretization of the SAS with $k_{max} = 1$ is particularly important since it represents the exact linear problem solution. Moreover, the linearized solution allows a comprehensive investigation of the error sources in the SAS, as described in Section 6.2.1.

Then, we proceed by considering T_p varying in the calculation of K and h_r and comparing the SAS results with well-known fixed-step numerical methods: explicit Euler, Heun, Ralston, and Runge-Kutta of 3rd, 4th and 5th order (all these methods were implemented by us). All calculations are performed on a computer with an Intel® Core™ i5-10400F CPU running at 2.9 GHz (6 cores, 12 threads), 64 GB RAM, and Windows 11 Pro 64-bit.

6.2 Model validation

The model (partial) validation is made by comparing the thermogravimetric analysis (TGA) data for calcination of kaolinite (Teklay et al., 2014) – see case study *b* – with model predictions. Validation is said to be partial because the TGA only partially represents the conditions of a MBR. For the SAS to mimic the operating conditions of the TGA, the following settings are made (see Medeiros et al., 2021): $\acute{t} \equiv z/v_p =$ TGA clock time, $v_p = v_f/\varepsilon$, h_f and h_r low enough (≈ 0) to nullify thermal exchanges with the wall, c_f sufficiently high (10^{10}) so that T_f does not change through heat exchange with the particles, but changes as a linear function of the heating rate and particle residence time $(= 298 + 40\acute{t})$, and T_w is changed to the equilibrium temperature $T_{eq,k}$, calculated for each k section.

As a kind of cross-validation, SAS is compared with FD – the solution of DM using Finite Differences –, and with the Semi-Analytical solution of Medeiros et al. (SA) (a description of DM can be found in Appendix A). In the FD, the DM is discretized using a second order approximation for the spatial

differential operators. The model was solved with the ODE23tb solver.

6.3 Stability

Given the semi-analytical character, the roots (eigenvalues) and form of the SAS are known. Thus, SAS stability analysis can be carried out in a simple way, by analyzing the signal of the roots and inspecting its implementation (Press et al., 1992).

6.4 Consistency and convergence

To test consistency, a methodology analogous to that for verifying an analytical solution is introduced: SAS in continuous variables is substituted into the model equations. Then, if the system of model equations is satisfied, consistency is demonstrated. This methodology is more general than that of Vanti et al. (2008) and Bertoli et al. (2015a), since in these works, given the simplicity of the models studied, the SAS in continuous variables can be obtained directly from the model equations (see comments in Section 3.1) – and, consequently, consistency is ensured –. If stability and consistency are demonstrated, SAS convergence is automatically guaranteed according to the Lax-Richtmyer equivalence theorem (Lax and Richtmyer, 1956).

6.5 SAS error analysis

Initially, we define ζ as a generic variable that represents T_f, T_p or X. Then, for ζ calculated with k_{max} intervals, the following SAS error expressions are written:

$$E^T_{\zeta;k_{max}}(\tau) \equiv \zeta_{k_{max}}(\tau) - \zeta(\tau) = E^R_{\zeta;k_{max}}(\tau) + E^L_{\zeta;k_{max}}(\tau) \tag{63}$$

$$\mathrm{RMSE}_{\zeta;kmax} \equiv \sqrt{\sum_{j=1}^{M} \frac{1}{M} \left(E_{\zeta;k_{max}}(\tau_j)\right)^2} \tag{64}$$

Where $E^T_{\zeta;k_{max}}$ is the total error, given by the sum of the machine rounding error, $E^R_{\zeta;k_{max}}$ (roundoff error), with the error due to model linearization, $E^L_{\zeta;k_{max}}$ (linearization error), and $\mathrm{RMSE}_{\zeta;k_{max}}$ is the Root Mean Squared Error (RSME). The following subsections present the analysis methodology for these types of error.

6.5.1 Roundoff error $\left(E^{R}_{\zeta;k_{max}}\right)$

In this work, roundoff errors are estimated using two independent methods: the first – known from the literature – is based on accounting for floating point operations; and the second – developed here – makes use of characteristics of SAS. These methods are described respectively below.

- Method *A* – Estimation based on expressions from the literature

The random and non-random round-off errors in the calculation of ζ can be estimated as a function of number of intervals from assessment of the number of arithmetic operations of each calculation. The code developed by Qian (2023) was used to calculate the number of arithmetic operations (FLOPS) for the SAS, considering an average (and constant) T_p in the calculation of h_r and K, for each k_{max} tested. Then, estimates of random and non-random roundoff errors were performed by multiplying the machine precision ($\epsilon_M = 2.220446049250313 \times 10^{-16}$) by FLOPS at the power ½ and 1, respectively (Press et al., 1992).

- Method *B* – Estimation based on SAS characteristics

SAS can provide an excellent estimate of this error if we consider that the linearized model solution is exact. If K and h_r are made constant – e.g., at an average temperature along the reactor –, SAS can be used to solve the linear problem. Estimating K and h_r at an average temperature, one has approximately the same order of magnitude for the arguments of the exponential functions and for the coefficients of the solution, in comparison with the non-linear problem. For the same number of intervals, the SAS can be programmed to perform approximately the same number of operations both on the linear problem and on the corresponding non-linear problem. For a given τ, the difference between the results of the linear problem, using $k_{max} = 1$ and $k_{max} = N$, is due only to the roundoff error. As a result of the previous considerations, it is concluded that an excellent estimate of $E^{R}_{\zeta;k_{max}}$ can be obtained from the difference between the results of the SAS for the linear problem with $k_{max} = 1$ and with $k_{max} = N$.

6.5.2 Linearization error $\left(E^{L}_{\zeta;k_{max}}\right)$

To evaluate the linearization error, the following iterative procedure is adopted:

(a) A set $S = \{k_{max_1}, k_{max_2}, \cdots, P\}$ of increasing k_{max} intervals is composed, assuming that for each element $E^R_{\zeta;k_{max}} \ll E^L_{\zeta;k_{max}}$, and that $E^L_{\zeta;P} \ll E^L_{\zeta;k_{max}\neq P}$;

(b) the $E^L_{\zeta;k_{max}}$ for calculations with k_{max} intervals is given approximately by the following expression:

$$E^L_{\zeta;k_{max}}(\tau_j) \cong \zeta_{k_{max}\neq P}(\tau_j) - \zeta_P(\tau_j); \tag{65}$$

(c) the RMSE for calculations with k_{max} intervals is given approximately by the following expression:

$$\text{RMSE}_{\zeta;k_{max}} \cong \sqrt{\sum_{j=1}^{M} \frac{1}{M} \left(\zeta_{k_{max}\neq P}(\tau_j) - \zeta_P(\tau_j)\right)^2}; \tag{66}$$

(d) the linearization error trend line is plotted as a function of k_{max};

(e) if the results agree with the assumptions in (a), the procedure ends, otherwise a new choice of S is made and the procedure is restarted.

6.6 Stiffness

Stiffness is a characteristic of interest in the integration of an ODE system and is normally quantified by the stiffness ratio (SR) (Davis, 1984). In the present study, the SR for the linearized model can be defined in the following form

$$\text{SR} \equiv \frac{\max_i |r_i|}{\min_i |r_i|}, \; i = 1, 2, 3 \tag{67}$$

Although the model under study is a nonlinear system of ODEs, whose stiffness may vary over time (Davis, 1984), SAS is based on "interval solutions of the linearized model" whose form is independent of them. Therefore, if for a given SR (say SR_1) it is possible to integrate the model equations keeping K and h_r constant – i.e., the linear problem –, then, the integration of the nonlinear problem can be guaranteed as long as $\text{SR}(\tau) < \text{SR}_1$ for $(0 \leq \tau \leq \tau_L)$. Therefore, to evaluate SAS with respect to system stiffness, the SR is varied over several orders of magnitude and the performance of SAS is compared with that of the fixed-step ODE integrators from Section 6.1 and with two implicit variable-step methods from MATLAB (MATLAB R2024b, The MathWorks, Inc.): ODE23s and ODE15s, which are specific to stiff problems. The variation in the order of magnitude of the SR is achieved through the variation of the pre-exponential

factor (A). This artificial variation can generate non-physical results – for example, negative absolute temperatures –, however, this does not interfere with this numerical analysis.

7. Results and discussion

7.1 Model verification

SAS is initially verified by comparison with the analytical solution of the linear (and simpler) model, and with results from other numerical methods. Case study *a* (Section 5) with the modifications: h_r and K evaluated at $T_p = 597.2$ K, is used in the comparison. Thus, following the methodology of Section 6.1, two discretization levels are considered, $k_{max} = 10^4$ and $k_{max} = 1$. As illustrated in Fig. 2, excellent agreement (within the machine error) was obtained for ζ at the reactor outlet, for the different discretization levels studied.

Insert Figure 2

Then, we proceed to investigate the SAS performance considering variable T_p in calculating h_r and K. Fig. 3 shows the predictions for ζ profiles – numerical solutions of Eqs. (10)-(15) – from SAS and the 4th order Runge-Kutta method, resulting in excellent agreement between the different solution methods.

Insert Figure 3

In Fig. 4, further comparisons for the conditions described for Fig. 3 are performed with other numerical methods (explicit Euler, Heun, Ralston, and Runge-Kutta of 3rd and 5th order), also showing excellent agreement. For the relative difference defined by Eq. (68), a maximum of $\mathcal{O}(10^{-1})\%$ was found for T_f and T_p.

$$\Delta\zeta\% = \frac{|\zeta^{\mathrm{OM}} - \zeta^{\mathrm{SAS}}|}{\zeta^{\mathrm{SAS}}} \times 100 \tag{68}$$

Insert Figure 4

Figure 5 presents a comparison of the computation time of different numerical methods, for integrating the model equations over the length of the reactor, under the conditions described in Fig. 4.

Insert Figure 5

As indicated in Fig. 5, the SAS calculation time is approximately half that observed in the solution by the explicit Euler method. The advantage of the SAS is, therefore, evident: not only is it unconditionally stable – unlike the explicit numerical methods that can diverge depending on the step size –, but it also requires significantly less computation time when compared with the other numerical methods. However, as will be demonstrated in Section 7.3.4, if $k_{max} < 10^2$, SAS behavior becomes erratic.

7.2 Model validation

Following the methodology described in Section 6.2, the (partial) validation of this model is performed by comparison with TGA data from Teklay et al. (2014) – case study *b* –. For a heating rate of 40 K/min, Fig. 6 shows the SAS results using the dehydroxylaxion kinetic parameters (K1 − K8) from Table 2 and the TGA data from Teklay et al. (2014).

Insert Table 2

Insert Figure 6

As seen in Fig. 6, despite the simplification in the kaolinite calcination kinetics – simplified in the analysis, to the kaolinite dehydroxylation step –, for sets K2, K3 and K6 there is a reasonable agreement between the model predictions and the TGA data, partially validating the model. Moreover, as can be noticed from Fig. 7(A), there is excellent agreement between SAS and SA on the TGA issue, reinforcing

the consistency of the results obtained herein. However, comprehensive validation of SAS requires comparison with MBR data.

Figure 7(B) shows a comparison between SAS and the baseline case of Teklay et al. (2014), for the evolution of particle temperature as a function of residence time when suddenly exposed to a hot gas environment (i.e., under an instantaneous heating condition, differently from the controlled heating used in the TGA test presented in Fig. 6) In this scenario, T_{pi} = 298.15 K, R_p = 50 μm, and T_g = 1,273.15 K. Moreover, Figs. 7(C)-(D) presents a comparison of the SAS with the SA and the FD, respectively, performed according to Section 6.2. All results consider case study *b*.

Insert Figure 7

As can be seen, the results agree satisfactorily, enabling cross-validation between the present model and the others mentioned. Note, however, that the model by Teklay et al. (2014) – more complex in the description of the phenomena in the solid phase and the chemical kinetics of the flash calcination of kaolinite – is intended for the simulation of the calcination of kaolinite in a fluidized bed reactor (for which $\acute{t}$ should be interpreted as the "clock" time). This good predictive ability of SAS compared to more complex models is discussed a little in section 7.4.

7.3 Numerical analysis

In this section, a numerical analysis of the SAS is developed, aiming at the following aspects: stability, consistency and convergence, roundoff and linearization errors, as well as the ability to solve stiff problems.

7.3.1 SAS stability

By definition, $\varphi_{k-1} > 1$ and $\mathrm{Py}'_{k-1} > 0$. Thus, from Eqs. (34c, d) and (36), we have $r_{l,k-1} < 0$ $(l = 1 - 3)$. Therefore, following the methodology in Section 6.3, it can be concluded that the implementation of SAS in the form of Eqs. (46)-(48) is unconditionally stable, since a perturbation on a

single value of ζ_{k-1} produces a variation in subsequent values that does not increase step by step, regardless of the value of $\Delta\tau$ (Gear, 1971).

7.3.2 Consistency and convergence

Following the methodology of Section 6.4, the SAS in continuous variables – Eqs. (54)-(61) – is substituted into the model equations, i.e., Eqs. (10)-(15). It is shown in Appendix B that by carrying out this substitution, each equation in the model is satisfied. Thus, for $\Delta\tau \to 0$, SAS converges to the exact solution and, therefore, consistency is demonstrated. Since the stability of SAS has already been demonstrated, these results allow us to conclude (according to Section 6.4) that SAS is a convergent numerical scheme.

7.3.3 Roundoff error

Figure 8(A) presents the estimates of absolute roundoff error for ζ, as a function of k_{max}, for case study *a,* considering h_r and K evaluated at $T_p = 597.2$ K. The results are presented according to the methods described in Section 6.5.1: *A* (markers), and *B* (solid and dashed lines for random and non-random round-off errors, respectively). Using method *B*, the roundoff error was estimated by comparing the SAS at each k_{max} considered (10^1 to 10^8) with the exact solution at $k_{max} = 1$.

Insert Figure 8

As can be seen, for $k_{max} > 10^4$ the values obtained with method *B* are located at intermediate points to those obtained with method A, thus demonstrating consistency.

Figure 8(B)-(D) presents the ζ profiles for the conditions described for Fig. 8(A) as a function of k_{max}. Interestingly, in Figs. 8(B)-(D) the estimated roundoff error presents regular behavior, only when $k_{max} > 10^3$. This is since for $k_{max} > 10^3$, SAS maintains a pattern in the ζ profiles, that is refined as k_{max} increases.

7.3.4 Linearization error

Figure 8(E) presents the estimates of the linearization error for ζ, as a function of k_{max}, for case study *a*. The results were obtained according to the methodology in Section 6.5.2, considering $P = 10^8$. For $k_{max} > 10^2$ the linearization error decreases as k_{max} increases, as expected, with a linear behavior in a log-log plot. For $k_{max} < 10^2$, however, the linearization error behavior is erratic, as observed in Fig. 8(B)-(D), i.e., the physics of the problem is not effectively captured in this discretization level. Only after a certain onset, in this case identified as $k_{max} > 10^2$, the actual profiles for ζ are adequately captured, and successive refinements are obtained as k_{max} increases, allowing for proper interpretation of the solution performance – in this case in terms of linearization error.

Figure 9(A) presents the root mean squared linearization error for T_f as a function of k_{max}^{-1} for the conditions described for Fig. 8(E). The calculations were performed following the methodology described in Section 6.5.2, considering $P = 10^8$ and, h_r and K varying with T_p.

Insert Figure 9

Figure 9(B)-(D) details in a semilogarithmic scale, the behavior of the linearization error for large values of k_{max}. As discussed in Appendix C, for very large values of k_{max}, exact knowledge of this behavior is only accessible through theoretical analysis. However, observing the behavior of $\mathrm{RMSE}_{\zeta;k_{max}}$ in these figures, one can consistently infer the theoretical results Eqs. (C1) and (C2).

Among the various functions proposed to adjust $\mathrm{RMSE}_{\zeta;kmax}$ as a function of k_{max}^{-1} (see Supplementary Material), the hyperbolic sine function

$$f(k_{max}^{-1}) = a\sinh(k_{max}^{-1}) \tag{69}$$

showed an $R^2 = 0.9999$ for all ζ, with $\mathrm{RMSE}_{\zeta;k_{max}}$ of 5.606×10^{-6}, 8.074×10^{-6} and 3.441×10^{-7} for $\zeta = T_f, T_p$ and X, respectively. This fitting function is interesting because it has the theoretical properties

P_1 and P_2 of Appendix C. Furthermore, as k_{max}^{-1} increases, $\text{RMSE}_{\zeta;k_{max}}$ exhibits compatible behavior. This is the case except for $k_{max} < 10^2$, as will be seen below.

As discussed earlier, the phenomena are properly described in Figs. 9(B)-(D) for $k_{max} > 10^2$, and refinement is obtained as k_{max} increases. Moreover, a limiting discretization level with $k_{max} = 10^7$ should be adopted considering an error control strategy with the machine error three orders of magnitude lower than the linearization error. From the previous results and Fig. 9, it can be concluded that the analysis meets item (e) of the methodology in Section 6.5.2 and can therefore be completed.

7.3.5 Stiffness ratio (SR)

Following the methodology of Section 6.6, Table 3 lists the order of magnitude of SR that the different numerical methods were able to integrate, for case study *a*, with the following modifications: A variable, $E = 1200\ \frac{\text{J}}{\text{mol}}$, and, h_r and K evaluated at $T_p = 697.2$ K.

Table 3 clearly shows the superior performance of SAS, followed by the implicit variable-step methods – ODE23s and ODE15s – and the other explicit fixed-step methods (Euler, Ralston, Heun, Runge-Kutta of 3rd, 4th, and 5th order). Notably, SAS was able to integrate for all tested SRs. Also, the implicit variable step methods – ODE23s and ODE15s – stand out for solving very stiff systems, with $\text{SR} = 10^{16}$. ODE23s is a single-step and implicit solver based on the modified Rosenbrock formula of order 2, designed for moderately stiff ODEs. On the other hand, ODE15s is a multi-step and implicit solver based on the variable-order backward differentiation formula (BDF) method, designed for stiff ODEs and differential-algebraic system of equations.

Figure 10 illustrates the behavior of calculation time for ODE23s and ODE15s, depending on the SR tests in Table 3

Insert Figure 10

Depending on the SR, the calculation time for ODE solvers can become very high. This can be easily seen in Fig. 10 where the ODE15s calculation time presents an exponential behavior.

In Tests 10, 11 and 12, with SR 8.57×10^{29}, 8.57×10^{30} and, 8.57×10^{31}, respectively, the ODE15s computation time was 0.179 s, 0.625 s and 9.582 s, respectively. To make the calculation time behavior clear, Test 13 (SR $= 8.57 \times 10^{32}$) was not shown in Figure 10. However, its calculation time was 676.73 s with 5,735,317 steps. It should then be considered notable that for SR $= 8.57 \times 10^{32}$, SAS integrated the system in 5.515 s with 100,000 intervals. Another point to be highlighted is that the highest SR integrated with SAS for this case study was 4.2864×10^{305}, with a computation time of 6.81365 s. This is a very significant result.

The exceptional performance of SAS can be explained based on its unconditional stability (Section 7.3.1) associated with a relatively small number of operations in each interval. Hence, SAS has the capability to address stiff problems both numerically and computationally.

7.4 Scale analysis for MBR model selection

Model selection must consider accuracy and required resources. Thus, the simplest model with sufficiently accurate results is indicated (Çengel and Ghajar, 2011). In the literature, there are several detailed studies on lumped model selection criteria for different types of moving bed heat exchangers (Depew and Farbar, 1963; Kern and Hemmings, 1978; Fan and Zhu, 1998; Saastamoinen, 2004; Haim and Kalman 2008; Bertoli et al., 2017, 2020). In the context of processes involving chemical reactions in the solid phase, the literature is less extensive: Pyle and Zaror (1984) studied the pyrolysis of solids at low temperatures and proposed the use of small B and small Py' as selection criterion to lumped parameter model for the solid phase. In their modeling, the temperature of the fluid was assumed constant and equal to that of the furnace wall. This assumption makes the model simpler than that discussed in the present study. Another work to be considered is that of Lédé and Authier (2015). These authors, studying the biomass fast pyrolysis, proposed $B_p < 0.1$ as selection criterion to lumped parameter model for the solid phase, where B_p is calculated at the initial conditions of the process.

As is evident, in the presence of chemical reactions, the analysis of the topic in question becomes more complex. Therefore, in this work, only an exploratory approach is carried out, based on scale analysis. Thus,

based on the model assumptions and the scales in Table 1, it can be said that the present model – to lumped parameters in both phases – is more suitable for systems with negligible mass transfer effects, and small Bi, $\mathrm{Da_{IV}}$ and Th^2, respectively. The choice of small values for these dimensionless numbers make the conduction scale t_1 (see Table 1) considerably smaller than the other particle phenomena scales. However, it is understood that this may be a very conservative criterion and therefore an initial assessment is carried out in the next section.

7.5 SAS selection criteria - quantitative analysis

To verify the previous statements based on the scale analysis, as well as to obtain some quantitative information about the SAS selection criteria, a comparative analysis of SAS with FD is developed. This analysis is conducted with Bi and $\mathrm{Da_{IV}}$, as variables and E_R as the response, which is the relative error between SAS and FD, defined for the particle temperature and for the conversion by the following expressions, respectively

$$E_{R,Tp}\% = \frac{|T_{ps} - T_c|}{T_p^{\mathrm{SAS}}} \times 100, \qquad E_{R,X}\% = \frac{|X_{ps} - X_c|}{X^{SAS}} \times 100 \tag{70a, b}$$

For the fluid temperature, the relative error, $\Delta T_f(\%)$, is given by Eq. (68).

Figure 11(A, B, C) shows the ζ profiles as a function of Fo' calculated by SAS and FD and the associated error between SAS and FD, Eq. (68) for T_f and, Eq. (70) for T_p and X. Fig. 11(D) shows the variation of B and $|\mathrm{Da_{IV}}|$ with Fo' and, Fig. 11(E) shows the variation of Py' and Th^2 with Fo'. These results were obtained for case study *a*, with the modifications: $T_w = 573.25$ K, $E = 100\,\frac{\mathrm{kJ}}{\mathrm{mol}}$ and $k_p = 1.4\,\frac{\mathrm{W}}{\mathrm{m{\cdot}K}}$.

Insert Figure 11

As can be seen in Fig. 11, for $B < 0.038$ and $|\mathrm{Da_{IV}}| < 1.5$, there is excellent agreement between the results of the two methods. The maximum relative error was 0.17%, 0.04%, and 6.3% for the particle temperature, fluid temperature, and conversion, respectively. As illustrated in Figure 11, the following

variations are also observed in the calculations: $14.8 \times 10^{-4} < \mathrm{Th}^2 < 10.3$ and $99.0 \times 10^{-4} < \mathrm{Py}' < 68.5 \times 10^{2}$.

Figure 12 shows the ζ profiles for case study *a* with the modifications: $E = 65.97\ \frac{\mathrm{kJ}}{\mathrm{mol}}$, $k_p = 0.1\ \frac{\mathrm{W}}{\mathrm{m{\cdot}K}}$ and $T_w = 573.25$ K, and Fig. 13 shows the ζ profiles for case study *a* with the modifications: $E = 88.7\ \frac{\mathrm{kJ}}{\mathrm{mol}}$, $k_p = 0.025\ \frac{\mathrm{W}}{\mathrm{m{\cdot}K}}$ and $T_w = 573.25$ K. It was chosen to vary these parameters to perform the analysis without changing the hydrodynamic behavior of the process.

Insert Figures 12 and 13

In Fig. 12, for $B < 0.53$ and $20 < |\mathrm{Da_{IV}}| < 2.0 \times 10^{5}$, the maximum relative error was 3.6%, 0.029%, and 12.7% for the particle temperature, fluid temperature, and conversion, respectively. As illustrated in Figure 12, the following variations are also observed in the calculations: $13.4 \times 10^{1} < \mathrm{Th}^2 < 12.5 \times 10^{5}$ and $11.4 \times 10^{-7} < \mathrm{Py}' < 10.6 \times 10^{-3}$.

In Fig. 13, for $B \cong 2$ and $0.01 < |\mathrm{Da_{IV}}| < 1975$, the maximum relative error was 8.86%, 0.21%, and 200% for the particle temperature, fluid temperature, and conversion, respectively. As illustrated in Figure 13, the following variations are also observed in the calculations: $70.1 \times 10^{-3} < \mathrm{Th}^2 < 13.2 \times 10^{3}$ and $43.0 \times 10^{-3} < \mathrm{Py}' < 80.6$.

In Figs. 11(A), 12(A) and 13(A), it is observed that $\Delta T_f(\%)$ remains below 3% and presents behavior like that of $E_{R,Tp}(\%)$. This behavior is attributed to the low values of t_4/t_5 (see Table 1): 0.08708 for all cases.

In Figs. 11(B) and 11(C), 12(B) and 12(C), and 13(B) and 13(C), it is observed that the particle temperature and conversion results using the SAS, are within the results of the FD. Even so, in Fig. (13), at low conversions, the relative conversion error is very high. Other aspects to be observed in Figs. 11(D), 12(D) and 13(D) are as follows: the profiles of B and T_p are qualitatively similar, which is due to the dependence of h_r on T_p; the profile of $|\mathrm{Da_{IV}}|$ has exponential behavior, which is due to the Arrhenius law

for the rate constant. From the results in Figures 11-13, it can be concluded that for small Bi, small $|\mathrm{Da_{IV}}|$ and small Th^2, the present model, Eqs. (10)-(15), is as accurate as the DM - as predicted by the scale analysis - and therefore the SAS can be used. However, in the calculations in Figs. 12 and 13, the large variation of $|\mathrm{Da_{IV}}|$ and Th^2, makes it extremely difficult to evaluate the effect of these dimensionless numbers on the observed errors (the same holds for Py' in Figs. 11 and 13). Furthermore, not only the ranges of variation must be considered, but also the way in which it occurs. Thus, the analysis proves to be complex and therefore, this question is addressed to future studies.

It is worth noting that even in the absence of chemical reactions, establishing rigorous criteria for the selection of lumped parameter models may require in-depth analysis, as for example in moving bed heat exchangers (see Bertoli et al., 2017, 2019).

8. Conclusion

The continuous search for improving and optimizing MBRs motivates research in modeling and simulation. This work contributes to this area by presenting a semi-analytical solution for a lumped parameter kinetic and heat transfer model of a tubular MBR, where a first-order chemical reaction occurs uniformly within the particles. The local analytical solution was implemented within the FAM framework, resulting in a simple numerical programming scheme that is consistent, unconditionally stable, can fast integrate very stiff systems ($\mathrm{SR} = 10^{305}$), and requires a minimum of computational resources. These capabilities demonstrate the effectiveness of SAS as a methodology suitable for both academic research and industrial applications. Consequently, it signifies a substantial advancement for the modeling and optimization of moving bed reactors. For the sake of completeness, the other primary contributions of this work are itemized below:

- Demonstrates the accuracy of the SAS in comparison with other methods.
- Develops a specific methodology for SAS error analysis.
- Demonstrates analytically the unconditional stability of SAS in the implemented form.
- Generalizes a previous method for proving consistency of SAS.

- Improves the physical understanding of model parameters through scale analysis.
- Performs model (partial) validation through comparison with experimental data.
- Presents a solution that can be used as a benchmark for MBR simulations.
- Develops an initial assessment of the parametric range of SAS applicability.

Acknowledgements

This study was financed in part by "Coordenação de Aperfeiçoamento de Pessoal de Nível Superior – CAPES" (Finance code 001) and received support from "Conselho Nacional de Desenvolvimento Científico e Tecnológico – CNPq" (313202/2021-4 – C.S. and 312247/2022-2 – N.P.), and from the University of Blumenau (FURB). S.L.B. is grateful to the financial support received from "Fundação de Amparo à Pesquisa e Inovação do Estado de Santa Catarina (FAPESC), Edital 20/2024". J. E. A. H. is grateful for the support of ANP PRH 11.1.

Nomenclature

A	pre-exponential factor, $\left(\frac{1}{\mathrm{s}}\right)$
A_p	particle area $= 4\pi R_p^2$, (m^2)
a_1	wall area per unit volume of the reactor $= \frac{2}{R}$, $\left(\frac{1}{m}\right)$
Bi	compound Biot number $= \mathrm{Bi}_p + \mathrm{Bi}_r$, $(-)$
Bi_p	particle Biot number for convection heat transfer $= \frac{3h_pR_p}{k_p}$, $(-)$
Bi_r	particle Biot number for radiation heat transfer $= \frac{3h_rR_p}{k_p}$, $(-)$
B	$= \frac{\mathrm{Bi}}{3} = B_p + B_r$, $(-)$
B_p	$= \frac{\mathrm{Bi}_p}{3}$, $(-)$
B_r	$= \frac{\mathrm{Bi}_r}{3}$, $(-)$
$b_{l,k-1}$	SAS coefficient defined by Eqs. (37a), (41a) and (42a), $(-)$

$b'_{l,k-1}$ modified SAS coefficient defined by Eqs. (37b), (41b) and (42b), $(-)$

C_A concentration of species A, $\left(\frac{\text{mol}}{\text{m}^3}\right)$

c specific heat at constant pressure, $\left(\frac{\text{J}}{\text{kg}\cdot\text{K}}\right)$

Da_{IV} Damköhler fourth number for a first order irreversible chemical reaction $= \frac{(-\Delta H_R)KC_{Ai}R_p^2}{k_p T_{pi}}$, $(-)$

Da_{dev} external thermal Damköhler number for pyrolysis/devolatilization, for convection heat transfer $= \frac{(-\Delta H_R)KC_{Ai}R_p}{3h_p T_{pi}}$, $(-)$

$\text{Da}_{\text{dev},k-1}$ $= \frac{(-\Delta H_R)K_{k-1}C_{Ai}R_p}{3h_p T_{pi}}$, $(-)$

D_p solids thermal diffusivity $= \frac{k_p}{\rho_p c_p}$, $\left(\frac{m^2}{\text{s}}\right)$

d_p particle diameter, (m)

E activation energy, $\left(\frac{\text{J}}{\text{mol}}\right)$

$E_{\zeta;kmax}$ error for ζ calculated with $kmax$ intervals, $(-)$

$E_{R,\zeta}$ relative error between SAS and FD for $\zeta = T_p, X$, defined by Eq. (70), $(-)$

Fo' modified Fourier number $= \frac{D_p \acute{t}}{R_p^2}$, $(-)$

g dimensionless heat source, defined by Eq. (5), $(-)$

g_{k-1} linearized dimensionless heat source defined by Eq. (21), $(-)$

ΔH_R enthalpy of reaction, $\left(\frac{\text{J}}{\text{mol}}\right)$

h_f fluid-wall convective heat transfer coefficient, $\left(\frac{\text{W}}{\text{m}^2\cdot\text{K}}\right)$

h_p fluid-particle convective heat transfer coefficient, $\left(\frac{\text{W}}{\text{m}^2\cdot\text{K}}\right)$

h_r wall-particle radiative heat transfer coefficient $= \sigma\epsilon_p\left(T_w^2 + T_p^2\right)\left(T_w + T_p\right)$, $\left(\frac{\text{W}}{\text{m}^2\cdot\text{K}}\right)$

$h_{r,k-1}$ $= \sigma\epsilon_p\left(T_w^2 + T_{p,k-1}^2\right)\left(T_w + T_{p,k-1}\right)$, $\left(\frac{\text{W}}{\text{m}^2\cdot\text{K}}\right)$

K apparent reaction rate constant $= Ae^{-\frac{E}{\Re T_p}}$, $\left(\frac{1}{\mathrm{s}}\right)$

K_{k-1} $= Ae^{-\frac{E}{\Re T_{p,k-1}}}$, $\left(\frac{1}{\mathrm{s}}\right)$

k interval index

k_{max} number of intervals in which the reactor is axially sectioned

k_p solids thermal conductivity, $\left(\frac{\mathrm{W}}{\mathrm{m \cdot K}}\right)$

L reactor length, (m)

$\dot{m}_f$ fluid mass flow rate $= \rho_f v_f \pi R^2$, $\left(\frac{\mathrm{kg}}{\mathrm{s}}\right)$

$\dot{m}_p$ solids mass flow rate $= \rho_p v_p (1-\varepsilon)\pi R^2$, $\left(\frac{\mathrm{kg}}{\mathrm{s}}\right)$

n_v particle number density $= \frac{6\dot{m}_p}{\rho_p v_p \pi^2 R^2 d_p^3} = \frac{1-\varepsilon}{V_p}$, $\left(\frac{1}{\mathrm{m}^3}\right)$

$\mathcal{O}(a)$ order a

P largest element of S, $(-)$

Py pyrolysis first number $= \frac{k_p}{\rho_p c_p R_p^2 K} = \mathrm{Th}^{-2}$, $(-)$

Py′ pyrolysis second number for convection heat transfer $= \frac{3h_p}{\rho_p c_p R_p K}$, $(-)$

Py'_{k-1} $= \frac{3h_p}{\rho_p c_p R_p K_{k-1}}$, $(-)$

R reactor inner radius, (m)

$\Re$ gas constant $= 8.314$ $\left(\frac{\mathrm{J}}{\mathrm{mol \cdot K}}\right)$

R_p particle radius, (m)

$\mathrm{RMSE}_{\zeta;k_{max}}$ linearization RMSE defined by Eq. (66), in units of ζ

r radial position within the particle, (m)

$r_{l,k-1}$ root defined by Eqs. (34) and (36), $(-)$

r_{ws} wall area / particulate phase area $= \frac{2R_p}{3R(1-\varepsilon)}$, $(-)$

S set defined in Section 6.5.2

T temperature, (K)

Th thermal Thiele modulus $= R_p\sqrt{\frac{K}{D_p}}$, $(-)$

$\acute{t}$ particle residence time $= \frac{z}{v_p}$, (s)

t_2 $\acute{t}$ scale defined in Table 1, (s)

V reactor volume, (m^3)

V_p particle volume $= \frac{4}{3}\pi R_p^3$, (m^3)

v_f superficial velocity of the conveyor fluid, $\left(\frac{m}{s}\right)$

v_p particle axial velocity, $\left(\frac{m}{s}\right)$

X reactant conversion, $(-)$

z axial spatial coordinate, (m)

Greek Symbols

α $= \alpha_f + \alpha_p = \alpha_p\omega$, $(-)$

α_f $= \alpha_p(\omega - 1)$, $(-)$

α_p $= \mathrm{Bi}_p\beta$, $(-)$

β capacity rate ratio $= \frac{\dot{m}_p c_p}{\dot{m}_f c_f} = \frac{\rho_p v_p c_p(1-\varepsilon)}{\rho_f v_f c_f}$, $(-)$

$\Delta\zeta\%$ relative difference of ζ between OM and SAS, defined by Eq. (68), $(-)$

$\Delta\tau$ dimensionless time step $= \frac{3h_p L}{\rho_p v_p c_p R_p k_{max}}$, $(-)$

ε void fraction $= 1 - \frac{\dot{m}_p}{\rho_p v_p \pi R^2}$, $(-)$

ϵ surface emissivity, $(-)$

ϵ_M machine precision = $2.220446049250313 \times 10^{-16}$, $(-)$

ζ generic variable $= T_f$, T_p or X, $(-)$

θ dimensionless temperature $= \frac{T-T_i}{T_{pi}}$, $(-)$

$\theta_f(\infty)$ defined by Eq. (16), $(-)$

$\theta_p(\infty)$ defined by Eq. (17), $(-)$

ξ dimensionless particle radial coordinate $= \frac{r}{R_p}$, $(-)$

ρ density, $\left(\frac{\mathrm{kg}}{\mathrm{m}^3}\right)$

σ Stefan-Boltzmann constant $= 5.6697 \times 10^{-8} \left(\frac{\mathrm{W}}{\mathrm{m}^2 \cdot \mathrm{K}^4}\right)$

τ dimensionless residence time $= \frac{3h_p}{\rho_p c_p R_p} \acute{t}$, $(-)$

τ_L dimensionless residence time at L, $(-)$

φ $= 1 + \frac{h_r}{h_p}$, $(-)$

φ_{k-1} $= 1 + \frac{h_{r,k-1}}{h_p}$, $(-)$

ω $= 1 + r_{ws} \frac{h_f}{h_p}$, $(-)$

Subscripts

f fluid

g gas

hom homogeneous

i inlet

j discrete point j in τ

k discrete point k in τ

l root index

p particle

$part$ particular

pm average taken over an interval, for the particle

pc	particle center
ps	particle surface
w	wall

Superscripts

L	linearization
OM	other method
R	machine rounding
T	total

Acronyms

C	cooling
DM	MBR distributed parameter model of Medeiros et al. (2018, 2021)
FAM	finite-analytic method
FD	finite difference method
H	heating
LHS	left-hand side
ODE	ordinary differential equation
MBR	moving bed reactor
RMSE	root mean squared error
SA	semi-analytical solution of Medeiros et al. (2018, 2021)
SAS	semi-analytical solution
SR	stiffness ratio
TGA	thermogravimetric analysis

References

[1] A.C.L. Lisbôa, Transferência de Calor em Leito de Arrasto de Xisto (Heat Transfer in a Moving Bed of Oil Shale), M.Sc. Thesis COPPE, Universidade Federal do Rio de Janeiro, Rio de Janeiro, 1987.

[2] S.L. Bertoli, Transferência de Calor Convectiva e Radiante em Leito de Arrasto (Radiant and Convective Heat Transfer in Moving Beds), M. Sc. Thesis COPPE, Universidade Federal do Rio de Janeiro, Rio de Janeiro, 1989.

[3] S.L. Bertoli, Radiant and convective heat transfer on pneumatic transport of particles: An analytical study, Int. J. Heat Mass Transf. 43 (2000) 2345–2363, https://doi.org/10.1016/S0017-9310(99)00280-X.

[4] E. Aylón, A. Fernández-Colino, R. Murillo, M.V. Navarro, T. García, A.M. Mastral, Valorisation of waste tyre by pyrolysis in a moving bed reactor, Waste Manage. 30 (2010) 1220-1224. https://doi.org/10.1016/j.wasman.2009.10.001.

[5] J.D. Martínez, N. Puy, R. Murillo, T. García, M.V. Navarro, A.M. Mastral, Waste tyre pyrolysis - A review, Renew. Sust. Energ. Rev. 23 (2013) 179–213. https://ideas.repec.org/a/eee/rensus/v23y2013icp179-213.html.

[6] A. Teklay, C. Yin, L. Rosendahl, M. Bøjer, Calcination of kaolinite clay particles for cement production: A modeling study, Cem. Concr. Res. 61–62 (2014) 11–19. https://doi.org/10.1016/j.cemconres.2014.04.002.

[7] A. Teklay, C. Yin, L. Rosendahl, L.L. Køhler, Experimental and modeling study of flash calcination of kaolinite rich clay particles in a gas suspension calciner, Appl. Clay Sci. 103 (2015) 10–19. https://doi.org/10.1016/j.clay.2014.11.003.

[8] A. Teklay, C. Yin, L. Rosendahl, Flash calcination of kaolinite rich clay and impact of process conditions on the quality of the calcines: A way to reduce CO2 footprint from cement industry, Appl. Energy 162 (2016) 1218–1224. https://doi.org/10.1016/j.apenergy.2015.04.127.

[9] J. E. Apolinar-Hernández, S. L. Bertoli, H. G. Riella, C. Soares, N. Padoin, An overview of low-temperature Fischer–Tropsch synthesis: market conditions, raw materials, reactors, scale-Up, process Intensification, mechanisms, and outlook, Energy & Fuels 38 (2024) 1-28. https://doi.org/10.1021/acs.energyfuels.3c02287.

[10] M. Shirzad, M. Karimi, J.A.C. Silva, A.E. Rodrigues, Moving bed reactors: Challenges and progress of experimental and theoretical studies in a century of research, Ind. Eng. Chem. Res 58 (2019) 9179-9198. https://doi.org/ 10.1021/acs.iecr.9b01136.

[11] W.D. Munro, N.R. Amundson, Solid-fluid heat exchange in moving beds, Ind. Eng. Chem. 42 (1950) 1481–1488, https://doi.org/10.1021/ie50488a014.

[12] P. K. Leung, D. Quon, A computer model for moving beds – chemical reaction in fluid phase only, Can. J. Chem. Eng. 43 (1965) 45–48. https://doi.org/10.1002/cjce.5450430109.

[13] S. L. Bertoli, C.M. Hackenberg, Um modelo de parâmetros distribuídos para a transferência de calor em leito de arrasto. III Encontro Nacional de Ciências Térmicas, in: Anais do III Encontro Nacional de Ciências Térmicas, v. II. p. 731-736, Itapema (Brazil), 1990.

[14] L.S. Fan, C. Zhu, Principles of Gas-Solid Flow, Cambridge University Press, Cambridge, MA, USA, 1998 https://doi.org/10.1017/CBO9780511530142

[15] J.J. Saastamoinen, Heat exchange between two coupled moving beds by fluid flow, Int. J. Heat Mass Transf. 47 (2004) 1535-1547, https://doi.org/10.1016/j.ijheatmasstransfer.2003.10.011.

[16] H.F. Meier, D. Noriler, S.L. Bertoli, A solution for a heat transfer model in a moving bed through the self-adjoint operator method, Lat. Am. Appl. Res. 39 (2009) 327–336, http://www.scielo.org.ar/scielo.php?script=sci_arttext&pid=S0327-07932009000400006&lng=es&nrm=iso.

[17] J.A. Almendros-Ibáñez, A. Soria-Verdugo, U. Ruiz-Rivas, D. Santana, Solid conduction effects and design criteria in moving bed heat exchangers, Appl. Therm. Eng. 31, (2011) 1200-1207, https://doi.org/10.1016/j.applthermaleng.2010.12.021

[18] S.L. Bertoli, J.A.B. Valle, A.G. Gerent Jr., J. Almeida, Heat transfer at pneumatic particle transport – limit solutions, Powder Technol. 232 (2012) 64–77, https:// //doi.org/10.1016/j.powtec.2012.07.050.

[19] S.L. Bertoli, J. de Almeida Jr., J.C.S.C. Bastos, V.R. Wiggers, M.K. Silva, G.J. Pacheco, Semi Analytical Solution of a Heat Transfer and Kinetic Models Applied in a Biomass Pyrolysis Reactor, AICHE Annual Meeting 2015, Salt Lake City, 2015a.

[20] S.L. Bertoli, J. de Almeida Jr., R.K. Decker, L. Ender, J. de Almeida, A.C. Lovatel, A numerical solution of a model for heat transfer in moving beds, Chem. Eng. Trans. 43 (2015b) 1567–1572, https://doi.org/10.3303/CET1543262.

[21] S.L. Bertoli, C.K. de Souza, J.C.S.C. Bastos, J. de Almeida, J. de Almeida Jr., S. Licodiedoff, V.R. Wiggers, Lumped parameter analysis criteria for heat transfer in a co-current moving bed with adiabatic walls, Powder Technol. 317 (2017) 381–390, https://doi.org/10.1016/j.powtec.2017.05.018.

[22] S.L. Bertoli, R. Tribess, V.A. Castamann, A. Lovatel, C.K. De Souza, Analytical solution of a heat transfer model for a tubular co-current diluted moving bed reactor with indirect heating and intraparticle gradients, Powder Technol. 351 (2019) 259–272, https://doi.org/10.1016/j.powtec.2019.04.001.

[23] S.L. Bertoli, J. De Almeida Jr., C.K. De Souza, A. Lovatel, N. Padoin, C. Soares, Lumped analysis criteria for heat transfer in a diluted co-current moving bed heat exchanger with isothermal walls, Powder Technol. 361 (2020) 1038–1059, https://doi.org/10.1016/j.powtec.2019.10.092.

[24] S.L. Bertoli, R. Tribess, N. de Souza, C.K. de Souza, M.G.R. Reiter, M.J. Gonçalves, A simple solution for heat transfer in triple tube heat exchanger, Heat Transf. Eng. 43 (2022) 1918-1945, https://doi.org/10.1080/01457632.2021.2022321.

[25] S.L. Bertoli, C.K. de Souza, M.J. Gonçalves, N. Padoin, C. Soares, Solution by the self-adjoint operator method for a model of a co/counter-current moving bed heat exchanger with heat losses,

Case Studies in Thermal Engineering (51) 2023, 103578, https://doi.org/10.1016/j.csite.2023.103578.

[26] S. L. Bertoli, C. K. de Souza, M. J. Gonçalves, N. Padoin, C. Soares, Limit Solutions for a Lumped Parameter Model of Heat Transfer in a Diluted and Indirectly Heated Co-Current/Counter-Current Moving Bed Heat Exchanger with Heat Loss to Surroundings, Applied Thermal Engineering (236) Part A,

2024, 121348, https://doi.org/10.1016/j.applthermaleng.2023.121348.

[27] W.J. Yang, Z.Y. Zhou, A.B. Yu, Particle scale studies of heat transfer in a moving bed, Powder Technol. 281 (2015) 99–111, https://doi.org/10.1016/j.powtec.2015.04.071.

[28] P.A. Isaza, Y. Cai, W.D. Warnica, M. Bussmann, Co-current and counter-current vertical pipe moving bed heat exchangers: analytical solutions, Int. J. Heat Mass Transf. 95 (2016) 1115–1128, https://doi.org/10.1016/j.ijheatmasstransfer.2015.12.043.

[29] L.I.S.V. Medeiros, J.C.S.C. Bastos, M.I.L. Krautler, J. De Almeida Jr., M.J. Gonçalves, H. F. Meier, S. L. Bertoli, Solução semianalítica de um modelo de transferência de calor em leito móvel com reação de primeira ordem na fase sólida, p. 842-845. In: São Paulo: Blucher, 2018. ISSN 2359-1757, DOI: 10.5151/cobeq2018-PT.0231.

[30] L.I.S.V. Medeiros, S.L. Bertoli, M.J. Gonçalves, T.G. Hoffmann, B.L. Angioletti, H.F. Meier, Semi-analytical solution of a nonlinear heat transfer model for a tubular cocurrent moving-bed reactor with a first-order chemical reaction in the solid phase, J. Heat Transfer 143 (2021) 1-11, https://doi.org/10.1115/1.4051278.

[31] R. Tribess, S.L. Bertoli, C.K. de Souza, M.G.R. Reiter, M.I. Krautler, M.J. Gonçalves, Analytical solution of a heat transfer model for a tubular co-current diluted moving bed heat exchanger with indirect heating and thermal losses to the environment, Chem. Eng. Commun. 209 (2022) 808-826, https://doi.org/10.1080/00986445.2021.1919882.

[32] J. de Almeida Jr, Solução Semianalítica de um Modelo de Transferência de Calor em Leito de Arrasto (Semi-analytical Solution of a Heat Transfer Model in Moving Beds), M. Sc. Thesis, University of Blumenau, Blumenau, 2016.

[33] S. M. Walas, Cinetica de Reacciones Químicas, McGraw-Hill Book Co., Madrid, 1965.

[34] C. J. Chen, P. Li, The finite-analytic method for steady-state and unsteady heat transfer problems, Nineteenth ASME/AIChE U.S. National Heat Transfer Conference, Orlando, FL, ASME Paper No. 80-HT-86, July 27–30, 1980.

[35] F. Civan, Practical implementation of the finite-analytic method, Appl. Math. Model. 19 (1995) 298–306. https://doi.org/10.1016/0307-904X(94)00031-Z.

[36] F. Civan, Practical finite-analytic method for solving differential equations by compact numerical schemes, Numer. Methods Partial Differential Eq. 25 (2009) 347-379. https://doi.org/10.1002/num.20346.

[37] J. de Almeida Jr, V.R. Wiggers, J.C.S.C. Bastos, C.K de Souza, F.R.W. Schmitz, S.L Bertoli, Solução Semianalítica Híbrida para Transferência de Calor com Reação Química Aplicada a um Reator de Pirólise de Biomassa a Parâmetros Distribuídos, in: Anais do Congresso Brasileiro de Engenharia Química. Fortaleza (Brazil), 2016.

[38] D.A. Lemos, L.I. Medeiros, J. de Almeida Jr, L.F. de Carvalho, C.K de Souza, S.L Bertoli, Solução Semianalítica de Um Modelo a Parâmetros Distribuídos para a transferência de calor em leito-móvel, in: Anais do Congresso Brasileiro de Engenharia Química. Fortaleza (Brazil), 2016.

[39] M. Ardestani, M.S. Sabahi, H. Montazeri, Finite analytic methods for simulation of advection-dominated and pure advection solute transport with reaction in porous media, Int. J. Environ. Res. 9 (2015) 197-204. https://doi.org/10.22059/IJER.2015.889.

[40] M.G. Vanti, S.L. Bertoli, S.H.L. Cabral, A.G. Gerent, P. Kuo-Peng, Semianalytic Solution for a Simple Model of Inrush Currents in Transformers, IEEE Transactions on Magnetics 44 (2008) 1270-1273. https://doi.org/ 10.1109/TMAG.2007.916245.

[41] E. Butkov, Mathematical Physics, Addison-Wesley, Reading [Mass.], USA, 1973.

[42] C.R. Wiley, L.C. Barret, Advanced Engineering Mathematics, 5th ed., McGraw-Hill, Singapore, 1990.

[43] V.G. Jenson, G.V. Jeffreys, Mathematical Methods in Chemical Engineering. London, Academic Press, New York, 1963. Internet resource.

[44] S.L. Bertoli, J. de Almeida Jr., J. de Almeida, A.C. Lovatel, J.R. Eleoterio, S.L. Schwertl, P.R. Brandt, The Importance of limit solutions and temporal and spatial scales in the teaching of transport phenomena, Rev. Ing. Matemáticas y Ciencias la Inf. la Corporación Univ. Repub. 3 (2016) 13–19, http://dx.doi.org/10.21017/rimci.2016.v3.n6.a10.

[45] S. Salvador, Pozzolanic properties of flash-calcined kaolinite: A comparative study with soak-calcined products, Cem. Concr. Res. 25 (1995) 102–112, https://doi.org/10.1016/0008-8846(94)00118-I.

[46] S. Sperinck, P. Raiteri, N. Marks, N., K. Wright, Dehydroxylation of kaolinite to metakaolin—a molecular dynamics study, J. Mater. Chem. 21 (2011) 2118–2125, https://doi.org/10.1039/C0JM01748E.

[47] D. Bridson, T.W. Davies, D.P. Harrison, Properties of flash-calcined kaolinite, Clays Clay Miner. 33 (1985) 258–260, https://doi.org/10.1346/CCMN.1985.0330313.

[48] R.C.T. Slade, T.W. Davies, H. Atakül, R.M. Hooper, D.J. Jones, Flash calcines of kaolinite: Effect of process variables on physical characteristics, J. Mater. Sci. 27 (1992) 2490–2500. https://doi.org/10.1007/BF01105062

[49] W.H. Press, S.A. Teukolsky, W.T. Vetterling, B.P. Flannery, Numerical Recipes in C: The Art of Scientific Computing, 2nd ed., Cambridge University Press, Cambridge, NY, USA, 1992.

[50] P.D. Lax, R.D. Richtmyer, Survey of the Stability of Linear Finite Difference Equations, Communications on Pure and Applied Mathematics (1956), 9, 267-293. https://doi.org/10.1002/cpa.3160090206

[51] H. Qian (2023). Counting the Floating Point Operations (FLOPS) (https://www.mathworks.com/matlabcentral/fileexchange/50608-counting-the-floating-point-operations-flops), MATLAB Central File Exchange. Retrieved September 21, 2023.

[52] M.C. Davis, Numerical methods and modeling for chemical engineers. John Wiley & Sons, New York, NY, USA, 1984.

[53] MATLAB version R2024b. Natick, Massachusetts: The MathWorks Inc., 2024.

[54] C.W. Gear, Numerical initial-value problems in ordinary differential equations, Prentice-Hall, Englewood Clifts, NJ, USA, 1971.

[55] Y.A. Çengel, A.J. Ghajar, Heat and mass transfer: fundamentals and applications, 4th ed., McGraw-Hill Inc., NY, USA, 2011.

[56] Depew, C.A., Farbar, L. (1963). Heat Transfer to pneumatically conveyed glass particles of fixed size, Trans. ASME J. Heat Transfer, 164-172. https://doi.org/10.1115/1.3686042

[57] J. Kern, J.W. Hemmings, On the analogy between the calorimeter problem and some granulate-fluid exchange process, Trans. ASME J. Heat Transf. 100 (1978) 319 – 323.

[58] M. Haim, H. Kalman, The effect of internal particle heat conduction on heat transfer analysis of turbulent gas-particle flow in a dilute state, Granul. Matter 10 (2008) 341-349. https://doi.org/10.1007/s10035-008-0093-3

[59] D.L. Pyle, C.A. Zaror, Heat transfer and kinetics in the low temperature pyrolysis of solids, Chem. Eng. Sci. 39 (1984) 147-158. https://doi.org/10.1016/0009-2509(84)80140-2.

[60] J. Lédé, O. Authier, Temperature and heating rate of solid particles undergoing a thermal decomposition. Which criteria for characterizing fast pyrolysis? J. Anal. Appl. Pyrolysis 113, (2015) 1-14. https://doi.org/10.1016/j.jaap.2014.11.013.

[61] J.H. Levy, H.J. Hurst, Kinetics of dehydroxylation, in nitrogen and water vapour, of kaolinite and smectite from Australian Tertiary oil shales, Fuel (1993), 72(6), 873-877. https://doi.org/10.1016/0016-2361(93)90006-O

[62] M. Bellotto, A. Gualtieri, G. Artioli, S. Clark, Kinetic study of the kaolinite-mullite reaction sequence. Part I: Kaolinite dehydroxylation, Physics and Chemistry of Minerals (1995), 22(4), 207-217. https://doi.org/10.1007/BF00202254

[63] J. Arcenegui-Troya, P.E. Sánchez-Jiménez, A. Perejón, L.A. Pérez-Maqueda, Relevance of particle size distribution to kinetic analysis: the case of thermal dehydroxylation of kaolinite, Processes 9 (2021) 1852. https://doi.org/10.3390/pr9101852

[64] A.E. Kassa, N.T. Shibeshi, B.Z. Tizazu, Kinetic analysis of dehydroxylation of Ethiopian kaolinite during calcination, J. Therm. Anal. Calorim. 147 (2022) 12837–12853. https://doi.org/10.1007/s10973-022-11452-y

[65] P. Ptáček, D. Kubátová, J. Havlica, J. Brandštetr, F. Šoukal, T. Opravil, The non-isothermal kinetic analysis of the thermal decomposition of kaolinite by thermogravimetric analysis, Powder Technol. 204 (2010a) 222–227. https://doi.org/10.1016/j.powtec.2010.08.004

[66] P. Ptáček, D. Kubátová, J. Havlica, J. Brandštetr, F. Šoukal, T. Opravil, Isothermal kinetic analysis of the thermal decomposition of kaolinite: the thermogravimetric study, Thermochim. Acta 501 (2010b) 24–29. https://doi.org/10.1016/j.tca.2009.12.018

Appendix A – MBR distributed parameter model (Medeiros et al., 2021)

The MBR model studied by Medeiros et al. (2021) (DM) is to distributed parameters in the particles and to lumped parameters in the fluid phase, and the assumptions on which it is based are the same as those in Section 2 of this study, except that the thermal conductivity of the particle is considered finite. The equations of DM are written below:

Governing equations

$$\frac{\partial X}{\partial \mathrm{Fo}'} = \mathrm{Th}^2(1-X) \tag{A1}$$

$$\frac{d\theta_f}{\mathrm{dFo}'} = \alpha_p\left(\theta_{ps} - \theta_p(\infty)\right) + \alpha\left(\theta_f(\infty) - \theta_f\right) \tag{A2}$$

$$\frac{\partial \theta_p}{\partial \mathrm{Fo}'} = \frac{1}{\xi^2}\frac{\partial}{\partial \xi}\left(\xi^2 \frac{\partial \theta_p}{\partial \xi}\right) + G \tag{A3}$$

Where $X = X(\xi, \mathrm{Fo}')$, $\theta_f = \theta_f(\mathrm{Fo}')$, $\theta_p = \theta_p(\xi, \mathrm{Fo}')$.

Particle boundary conditions

$$\text{At } \xi = 0,\ \text{Fo}' > 0:\ \left.\frac{\partial \theta_p}{\partial \xi}\right|_{(0,\text{Fo}')} = 0 \tag{A4}$$

$$\text{At } \xi = 1,\ \text{Fo}' > 0:\ -\left.\frac{\partial \theta_p}{\partial \xi}\right|_{(1,\text{Fo}')} = B\left(\theta_{ps} - \theta_p(\infty)\right) - B_p\left(\theta_f - \theta_f(\infty)\right) \tag{A5}$$

And conditions at the reactor entrance

$$\text{At Fo}' = 0, \forall\, \xi:\ X(\xi, 0) = 0 \tag{A6}$$

$$\text{At Fo}' = 0:\ \theta_f(0) = 0 \tag{A7}$$

$$\text{At Fo}' = 0, \forall\, \xi:\ \theta_p(\xi, 0) = 0 \tag{A8}$$

In the above equations, $\theta_f(\infty)$ and $\theta_p(\infty)$ are given by Eqs. (16) and (17), respectively, and G is the dimensionless heat source term due to a first order irreversible chemical reaction

$$G = \text{Da}_{\text{IV}}\,(1 - X) \tag{A9}$$

Where $G = G(\xi, \text{Fo}')$, and the reaction rate constant is dependent on the temperature within the particle, according to the Arrhenius equation:

$$K\left(\theta_p(\xi, \text{Fo}')\right) = A\exp\left(\frac{-E}{\Re\, T_p}\right) = A\exp\left(\frac{-E}{\Re T_{pi}(\theta_p + 1)}\right) \tag{A10a, b}$$

Medeiros et al. (2018, 2021) semi-analytically solved this model introducing the additional simplification of constant rate inside the particle in each interval – calculated at the corresponding volumetric average particle temperature –. In the present study, this simplification is not made, and the model equations are solved using the Finite Difference (FD) method, as described in Section 6.2.

Appendix B – Verification of SAS in continuous variables

Initially, it is easy to see that the boundary conditions Eqs. (13)-(15) are satisfied by Eqs. (53)-(55) and, to verify the governing equations, we substitute into Eqs. (10)-(12) the solution in continuous variables, Eqs. (53)-(60):

- Substituting Eq. (53) in the LHS of Eq. (10) and developing, we have

$$\frac{dX(\tau)}{d\tau} = -r_3 e^{\int_0^\tau r_3 d\tau} = r_3(X(\tau) - 1) = \frac{1 - X(\tau)}{\text{Py}'} \equiv \text{RHS of Eq. (10)} \tag{B1a – d}$$

- Substituting Eq. (54) in the LHS of Eq. (11) and developing, we have

$$\frac{1}{\beta}\frac{d\theta_f(\tau)}{d\tau} = \frac{1}{\beta}\sum_{l=1}^{3} r_l b_l e^{r_l\tau} = \frac{1}{\beta}\left(r_1 \frac{b_3(r_3-r_2)e^{r_3\tau}+(\beta\omega+r_2)\left(\theta_f(\tau)-\theta_f(\infty)\right)-\beta\left(\theta_p(\tau)-\theta_p(\infty)\right)}{r_2-r_1} + \right.$$

$$\left. r_2 \frac{b_3(r_3-r_1)e^{r_3\tau}+(\beta\omega+r_1)\left(\theta_f(\tau)-\theta_f(\infty)\right)-\beta\left(\theta_p(\tau)-\theta_p(\infty)\right)}{r_1-r_2} + r_3 b_3 e^{r_3\tau} \right) = \theta_p(\tau) - \theta_p(\infty) + \qquad \text{(B2a – d)}$$

$$\omega\left(\theta_f(\infty) - \theta_f(\tau)\right) \equiv \text{RHS of Eq. (11)}$$

- Substituting Eq. (55) in the LHS of Eq. (12) and developing, we have

$$\frac{d\theta_p(\tau)}{d\tau} = \frac{1}{\beta}\sum_{l=1}^{3} r_l^2 b_l e^{r_l\tau} + \omega\sum_{l=1}^{3} r_l b_l e^{r_l\tau} = \frac{1}{\beta}\sum_{l=1}^{3} r_l^2 b_l e^{r_l\tau} + \omega\frac{d\theta_f(\tau)}{d\tau} =$$

$$\frac{r_3^2-(r_1+r_2)r_3+r_1r_2}{\beta} b_3 e^{r_3\tau} - \left(\omega(r_1+r_2) + \frac{r_1r_2}{\beta}\right)\left(\theta_f(\tau) - \theta_f(\infty)\right) - (r_1+r_2)\left(\theta_p(\tau) - \right.$$

$$\left.\theta_p(\infty)\right) + \omega\frac{d\theta_f(\tau)}{d\tau} = g(\tau) + (\beta\omega^2+1)\left(\theta_f(\tau) - \theta_f(\infty)\right) + (\beta\omega+\varphi)\left(\theta_p(\tau) - \qquad \text{(B3a – e)}$$

$$\left.\theta_p(\infty)\right) + \omega\left(\beta\omega\left(\theta_f(\infty) - \theta_f(\tau)\right) + \beta\left(\theta_p(\tau) - \theta_p(\infty)\right)\right) = g(\tau) + \theta_f(\tau) -$$

$$\theta_f(\infty) - \varphi\left(\theta_p(\tau) - \theta_p(\infty)\right) \equiv \text{RHS of Eq. (12)}$$

Therefore, the SAS in continuous variables satisfies the governing equations and the boundary conditions, thus constituting an exact representation - in integral form - of the system of model equations. This result is, therefore, proof of the consistency of the solution.

Appendix C – Properties of interest of the SAS linearization error for $k_{max} \to \infty$

As seen in Section 6.5.2, it is of interest to know the behavior of the SAS linearization error as a function of the number of intervals. However, for very large values of k_{max}, it is difficult at present - due to the large associated machine error or even technological limitations - to know exactly this behavior using only computational resources. Thus, the theoretical analysis of the SAS for this limit reveals the following properties of interest: $E^L_{\zeta;k_{max}}$

$$P_1 : \lim_{kmax\to\infty} E^L_{\zeta;kmax} = 0 \qquad \text{(C1)}$$

which follows immediately from the results in Appendix B; and

$$P_2: \lim_{kmax\to\infty}\left(\mathcal{O}\left(\frac{dE^L_{\zeta,kmax}}{dk^{-1}_{max}}\right) < \mathcal{O}(k^2_{max})\right) \tag{C2}$$

as a necessary result so that the following limit can be zero

$$\lim_{kmax\to\infty}\frac{dE^L_{\zeta,kmax}}{dk_{max}} = -\lim_{kmax\to\infty}\left(k^{-2}_{max}\frac{dE^L_{\zeta,kmax}}{dk^{-1}_{max}}\right) = 0 \tag{C3}$$

Note that the previous properties P_1 and P_2 are extended to $\mathrm{RMSE}_{\zeta;k_{max}}$.

Table Captions

Table 1: t' scales of phenomena for co-current vertical MBR

Table 2: Kinetic parameters for kaolinite dehydroxylation from different sources.

Table 3: Performance of different ODE solvers at different SR, for integration of model equations along the length of the reactor, for case study a, with the following modifications: A variable, $E = 1200\ \frac{\text{J}}{\text{mol}}$ and, h_r and K evaluated at $T_p = 697.2$ K.

Figure Captions

Figure 1: Schematic representation of the co-current moving-bed reactor and the differential control volume considered for the analysis.

Figure 2: ζ at L, calculated with $k_{max} = 10^4$ and $k_{max} = 1$, for case study *a* with the modifications: h_r and K evaluated at $T_p = 597.2$ K.

Figure 3: ζ profiles calculated with SAS ($k_{max} = 10^4$) and 4th order Runge-Kutta method with fixed step size, for case study *a* with the modifications: h_r and K considered to vary with T_p.

Figure 4: ζ profiles (A) − (J); $\Delta\zeta\%$ profiles (K, L). Profiles for case study *a* with the modifications: h_r and K considered to vary with T_p. In all cases, $k_{max} = 10^4$.

Figure 5: Computation time of the different methods used to integrate the model equations over L. All simulations were based on case study *a* with h_r and K varying with T_p. In all cases, $k_{max} = 10^4$.

Figure 6: Comparison of model predictions with TGA data (Teklay et al., 2014) at the heating rate of 40 K/min.

Figure 7: (A) SAS results for conversion compared with TGA data from Teklay et al. (2014) (solid black line) and with SA. (B)-(D) SAS results for particle temperature, and results from Teklay et al. (2014), SA and FD, respectively, for the central and surface temperature of the particle. All results for case study *b*.

Figure 8: (A) Estimates of absolute round-off error for ζ (markers), at $z = L$ (except X, evaluated at $L/2$), as a function of k_{max}. Solid and dashed lines for random and non-random round-off errors, respectively. (B)-(D) ζ profiles for $k_{max} \leq 10^3$. (E) Estimates of linearization error for ζ (markers), at $z = L$ (except X, evaluated at $L/2$), as a function of k_{max}. All results for case study *a,* considering h_r and K evaluated at $T_p = 597.2$ K in (A) and h_r and K varying with T_p in (B)-(E).

Figure 9: (A) Root mean squared linearization error (Eq. (66)) for T_f as a function of the reciprocal of the number of intervals, considering $P = 1 \times 10^8$. (B)-(D) Fitting by the hyperbolic sine function of the root mean squared linearization error for ζ. All results for case study *a,* considering h_r and K evaluated at $T_p = 597.2$ K.

Figure 10: Number of integration steps (bar chart) and computational calculation time (red line) for the ODE23s and ODE15s solvers, as a function of SR tests described in Table 3. All results for case study *a,* considering: A variable, $E = 1200 \ \frac{\text{J}}{\text{mol}}$ and, h_r and K evaluated at $T_p = 697.2$ K.

Figure 11: (A) Fluid temperature profiles from FD (black line) and SAS (green line), with the associated error, Eq. (68); (B)-(C) Particle temperature and conversion profiles obtained from FD (black lines) and SAS (green line), along with their respective relative errors, Eq. (70a) and, Eq. (70b); (D) $|\text{Da}_{\text{IV}}|$ and B profiles as a function of Fo'; (E) Py' and Th^2profiles as a function of Fo'. Calculations for case study a with the modifications: $E = 100 \ \frac{\text{kJ}}{\text{mol}}$ and $k_p = 1.4 \ \frac{\text{W}}{\text{m·K}}$.

Figure 12: (A) Fluid temperature profiles from FD (black line) and SAS (green line), with the associated error, Eq. (68); (B)-(C) Particle temperature and conversion profiles obtained from FD (black lines) and SAS (green line), along with their respective relative errors, Eq. (70a) and, Eq. (70b); (D) $|\text{Da}_{\text{IV}}|$ and B

profiles as a function of Fo'; (E) Py' and Th^2profiles as a function of Fo'. Calculations for case study a with the modifications: $E = 65.97\ \frac{\mathrm{kJ}}{\mathrm{mol}}$ and $k_p = 0.1\ \frac{\mathrm{W}}{\mathrm{m{\cdot}K}}$.

Figure 13: (A) Fluid temperature profiles from FD (black line) and SAS (green line), with the associated error, Eq. (68); (B)-(C) Particle temperature and conversion profiles obtained from FD (black lines) and SAS (green line), along with their respective relative errors, Eq. (70a) and, Eq. (70b); (D) $|\mathrm{Da}_{\mathrm{IV}}|$ and B profiles as a function of Fo'; (E) Py' and Th^2profiles as a function of Fo'. Calculations for case study a with the modifications: $E = 88.7\ \frac{\mathrm{kJ}}{\mathrm{mol}}$ and $k_p = 0.025\ \frac{\mathrm{W}}{\mathrm{m{\cdot}K}}$.

Table 1

Scale	Associated phenomenon
$t_1 \equiv \frac{R_p^2}{D_p}$	heat conduction at a distance R_p within the particle
$t_2 \equiv \frac{\rho_p c_p R_p}{3h_p}$	H of the particle by fluid-particle convection
$t_3 \equiv \frac{\rho_p c_p R_p}{3h_r}$	H of the particle by wall-particle radiation heat transfer
$t_4 \equiv \frac{\rho_f c_f v_f}{n_v A_p h_p v_p}$	C of the fluid by fluid-particle convection
$t_5 \equiv \frac{\rho_f v_f c_f}{a_1 h_f v_p}$	H of the fluid by fluid-wall convection
$t_6 \equiv \frac{\rho_p c_p T_{pi}}{(-\Delta H_R) K C_{Ai}}$	H of the particle by the first-order chemical reaction
$\tau_7 \equiv \frac{1}{K}$	first order chemical reaction in the solid phase

Table 2

Set	E (kJ/mol)	A (s^{-1})	Ref.
K1	163	2.00×10^{12}	Levy and Hurst (1993)
K2	193	1.00×10^{9}	Bellotto et al. (1995)
K3	180	6.30×10^{9}	Teklay, Yin and Rosendahl (2016)
K4	176	1.66×10^{11}	Teklay et al. (2014)
K5	99.6	9.00×10^{9}	Arcenegui-Troya et al. (2021)
K6	237.6	2.46×10^{9}	Kassa et al. (2022)
K7	222	1.00×10^{8}	Ptácek et al. (2010a)
K8	202	2.90×10^{15}	Ptácek et al. (2010b)

Table 3

Test No.	Kinetic Parameters		SR	Numerical Methods								SAS[a]
	E (J/mol)	A (1/s)		EE[a]	Rlst[a]	Heun[a]	RK3[a]	RK4[a]	RK5[a]	ODE23s[b]	ODE15s[b]	
1	1200	10^3	8.5728×10^2	●	●	●	●	●	●	●	●	●
2		10^4	8.5728×10^3	●	●	●	●	●	●	●	●	●
3		10^5	8.5728×10^4						●	●	●	●
4		10^6	8.5728×10^5							●	●	●
5		10^{10}	8.5728×10^9							●	●	●
6		10^{11}	8.5728×10^{10}							●	●	●
7		10^{12}	8.5728×10^{11}							●	●	●
8		2×10^{16}	1.7146×10^{16}							●	●	●
9		10^{25}	8.5728×10^{24}								●	●
10		10^{30}	8.5728×10^{29}								●	●
11		10^{31}	8.5728×10^{30}								●	●
12		10^{32}	8.5728×10^{31}								●	●
13		10^{33}	8.5728×10^{32}								●	●
14		10^{35}	8.5728×10^{34}									●

[a] The simulations were carried out with $k_{max} = 10^5$.

[b] The ODE23s and ODE15s solvers are implicit variable-step methods.

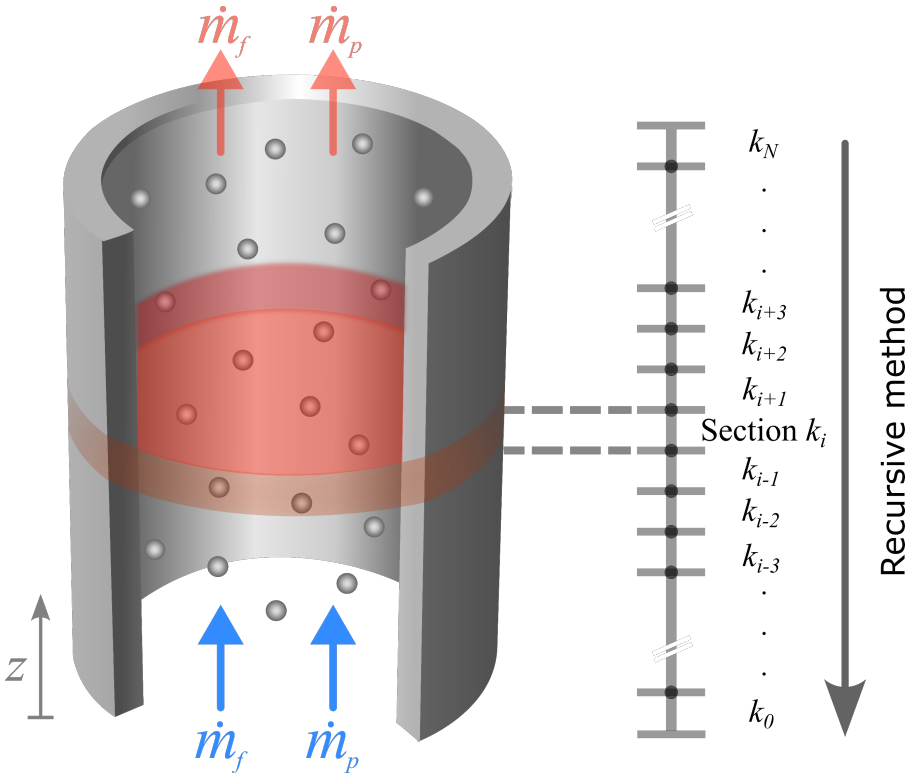

Figure 1

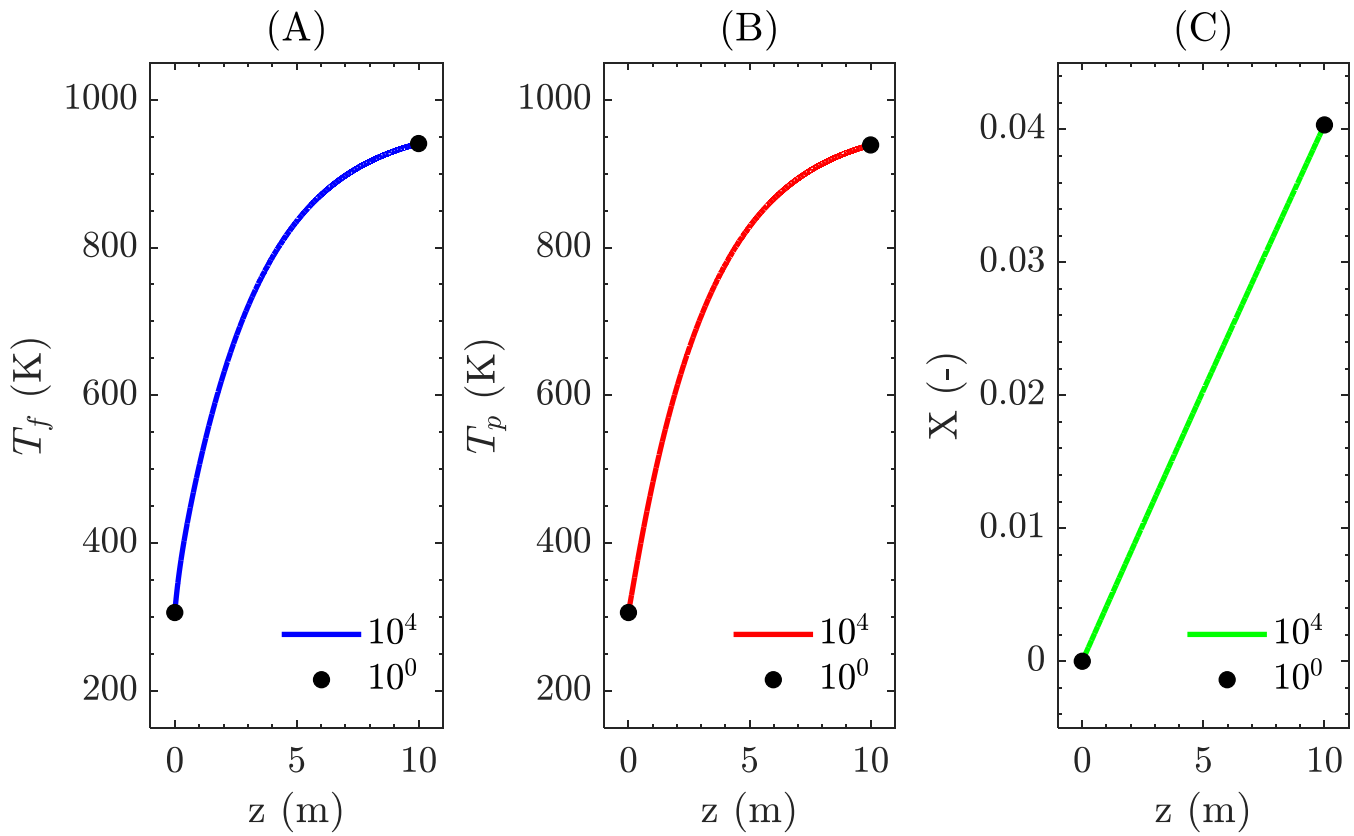

Figure 2

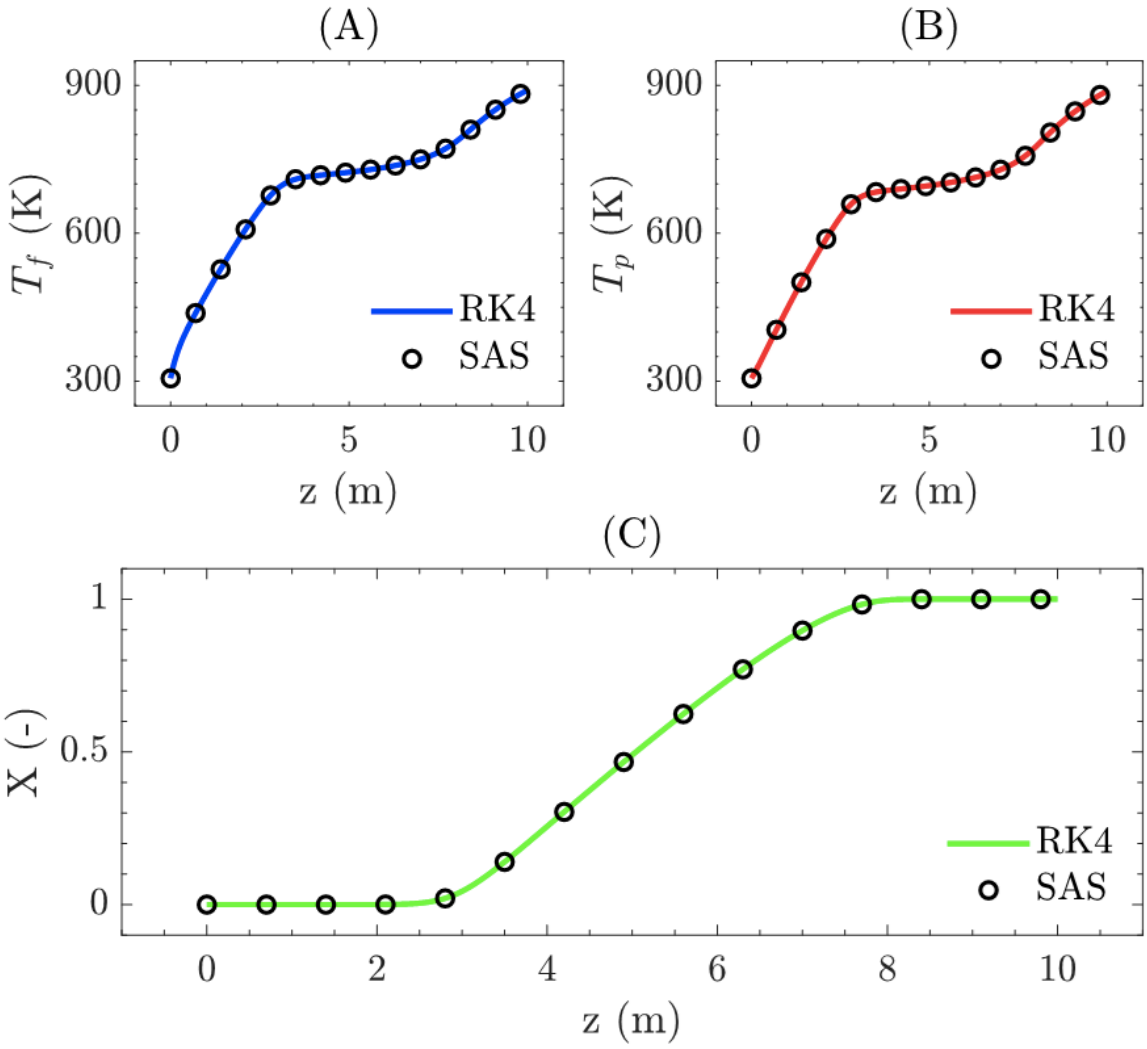

Figure 3

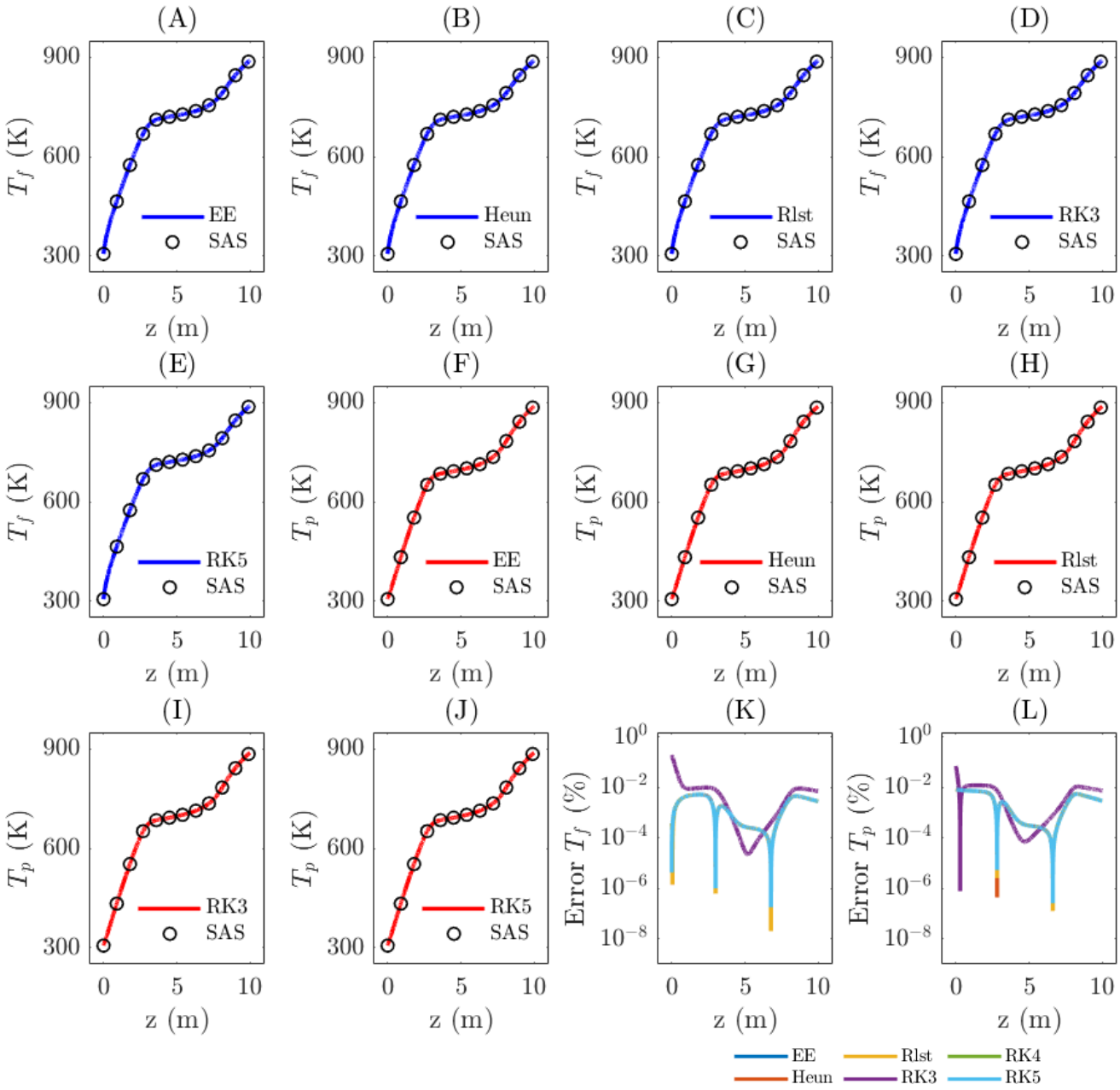

Figure 4

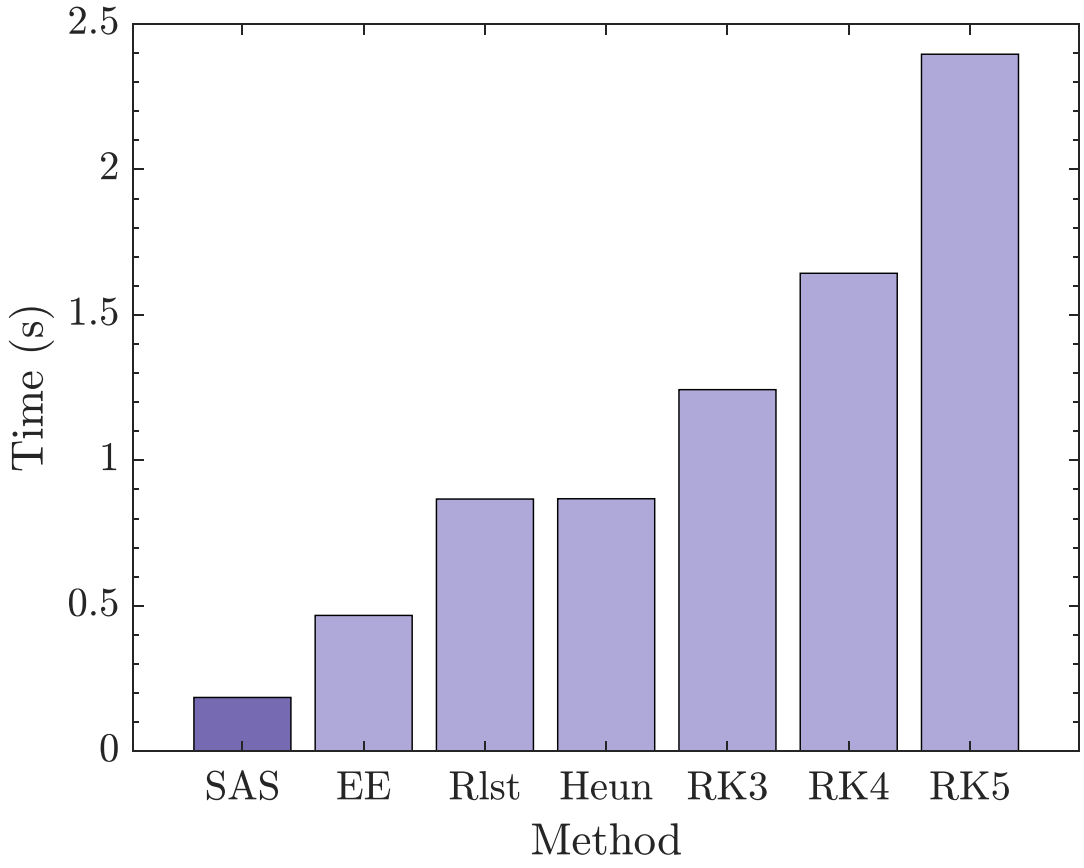

Figure 5

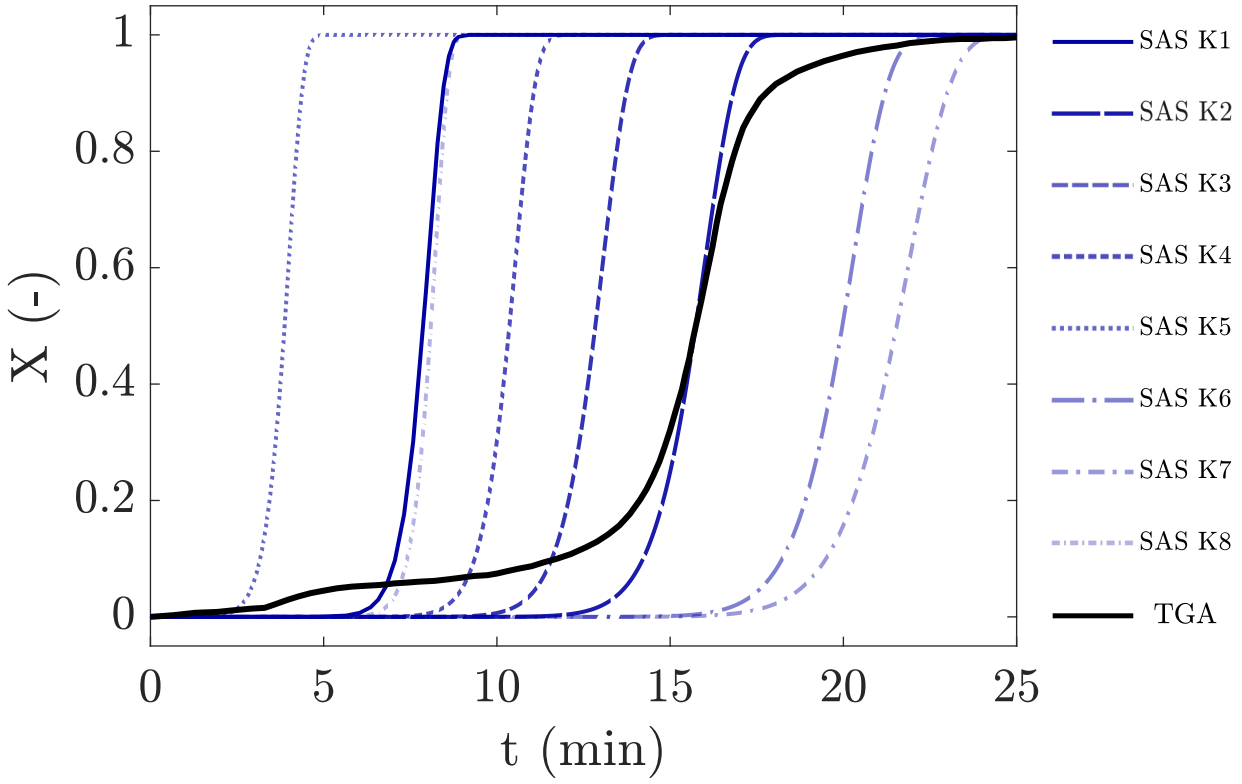

Figure 6

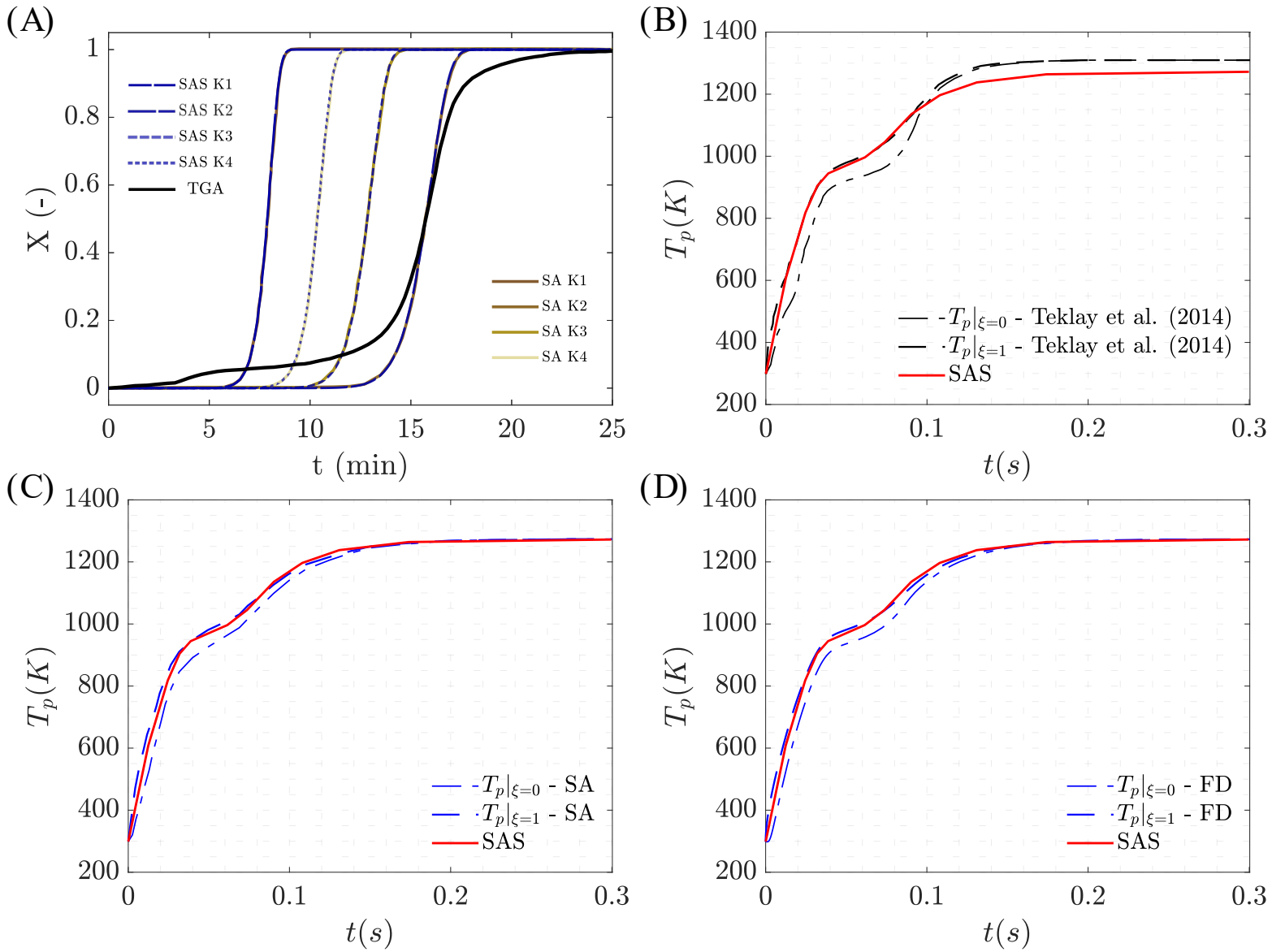

Figure 7

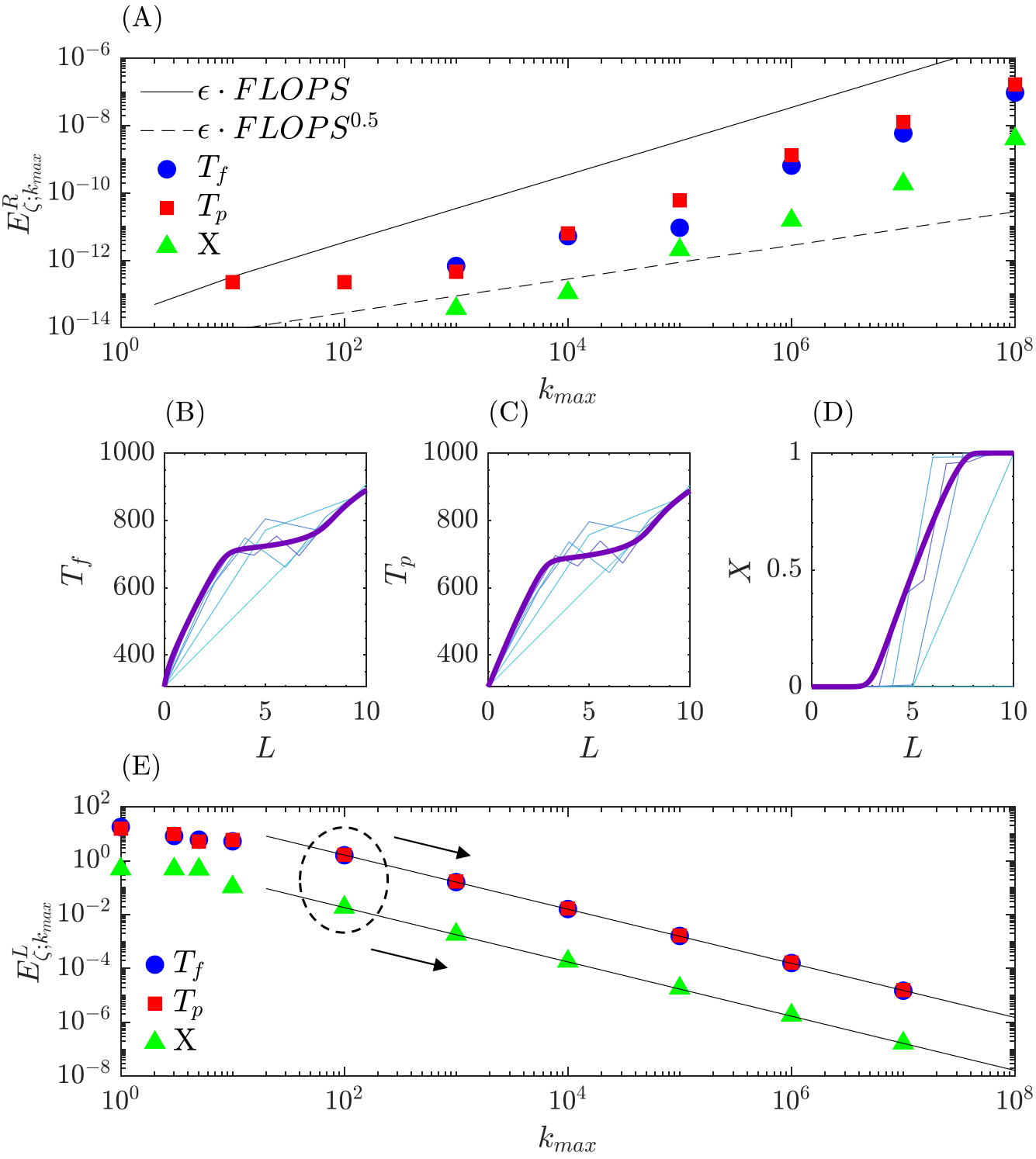

Figure 8

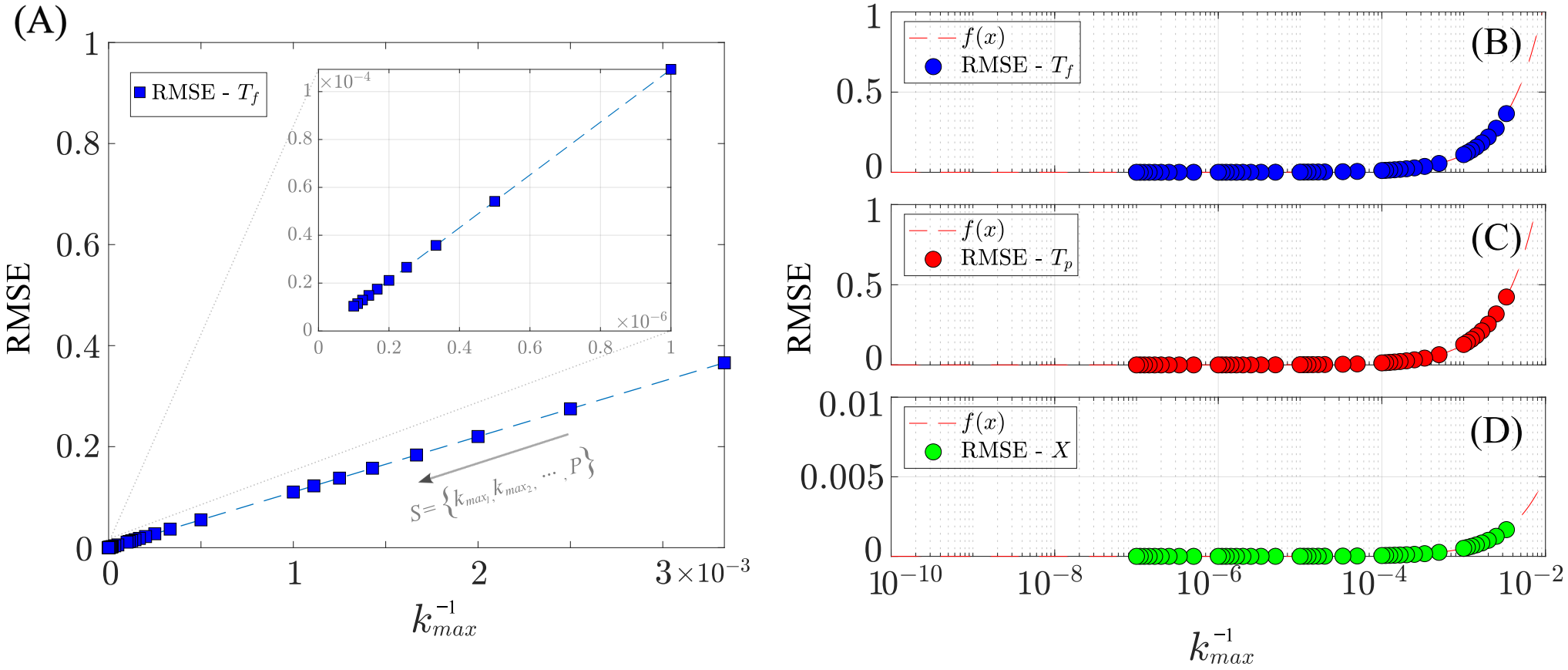

Figure 9

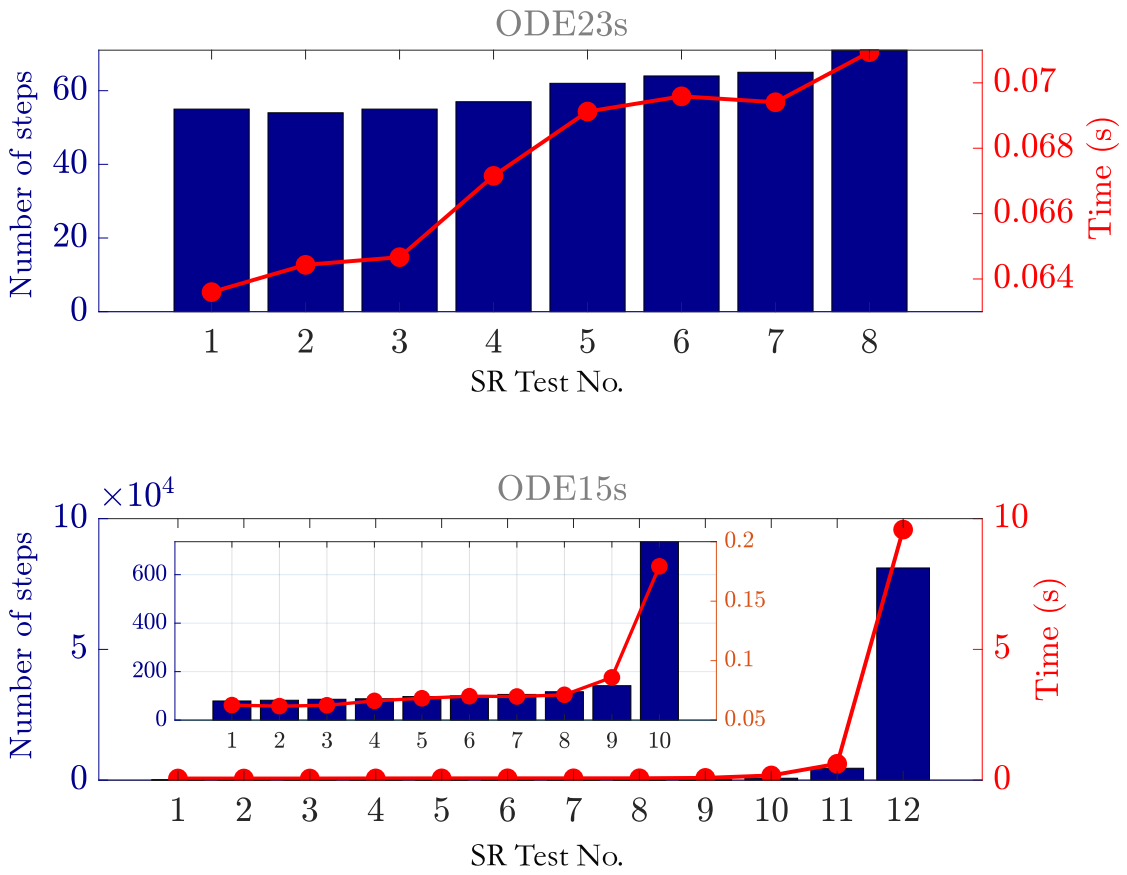

Figure 10

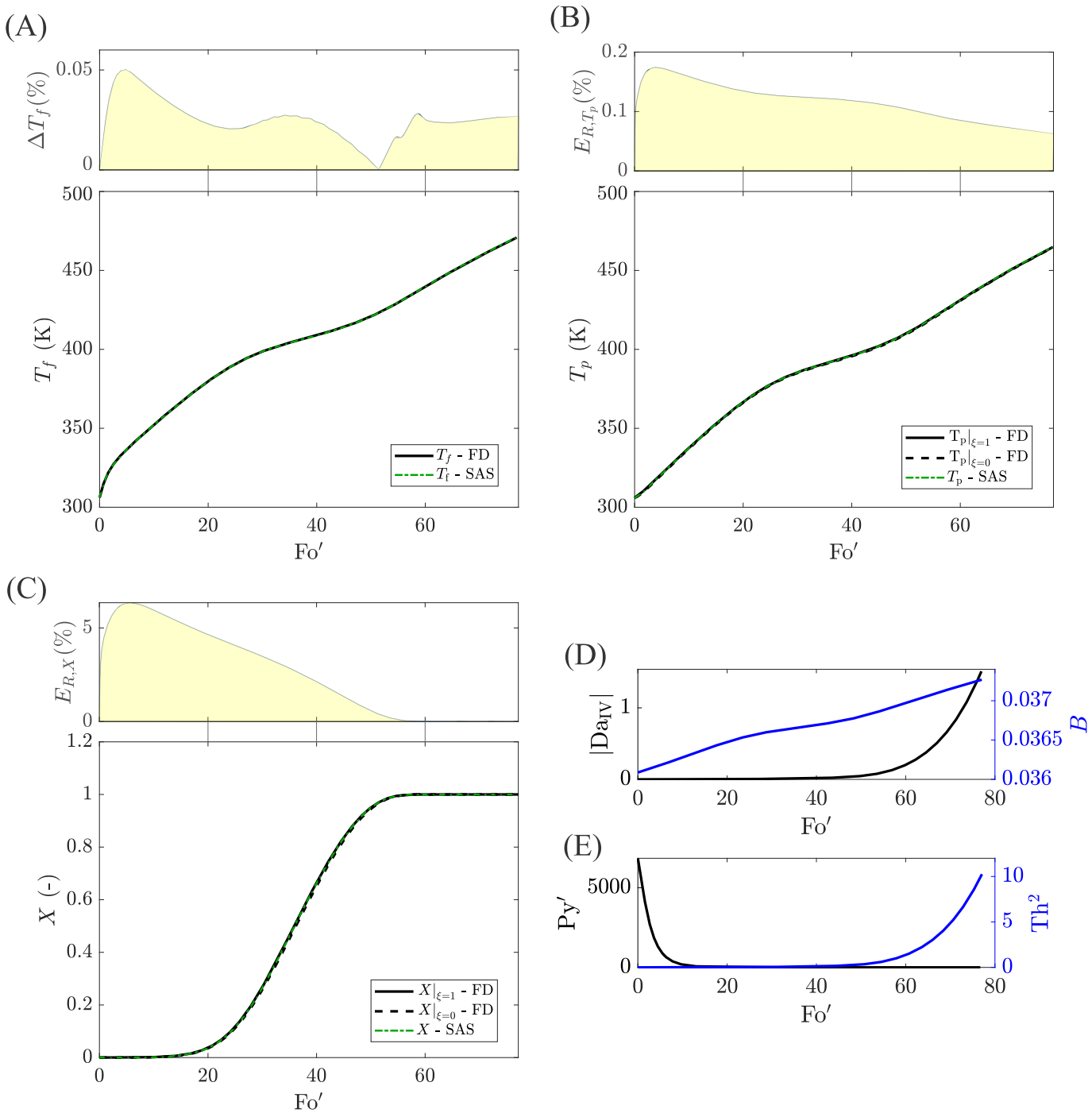

Figure 11

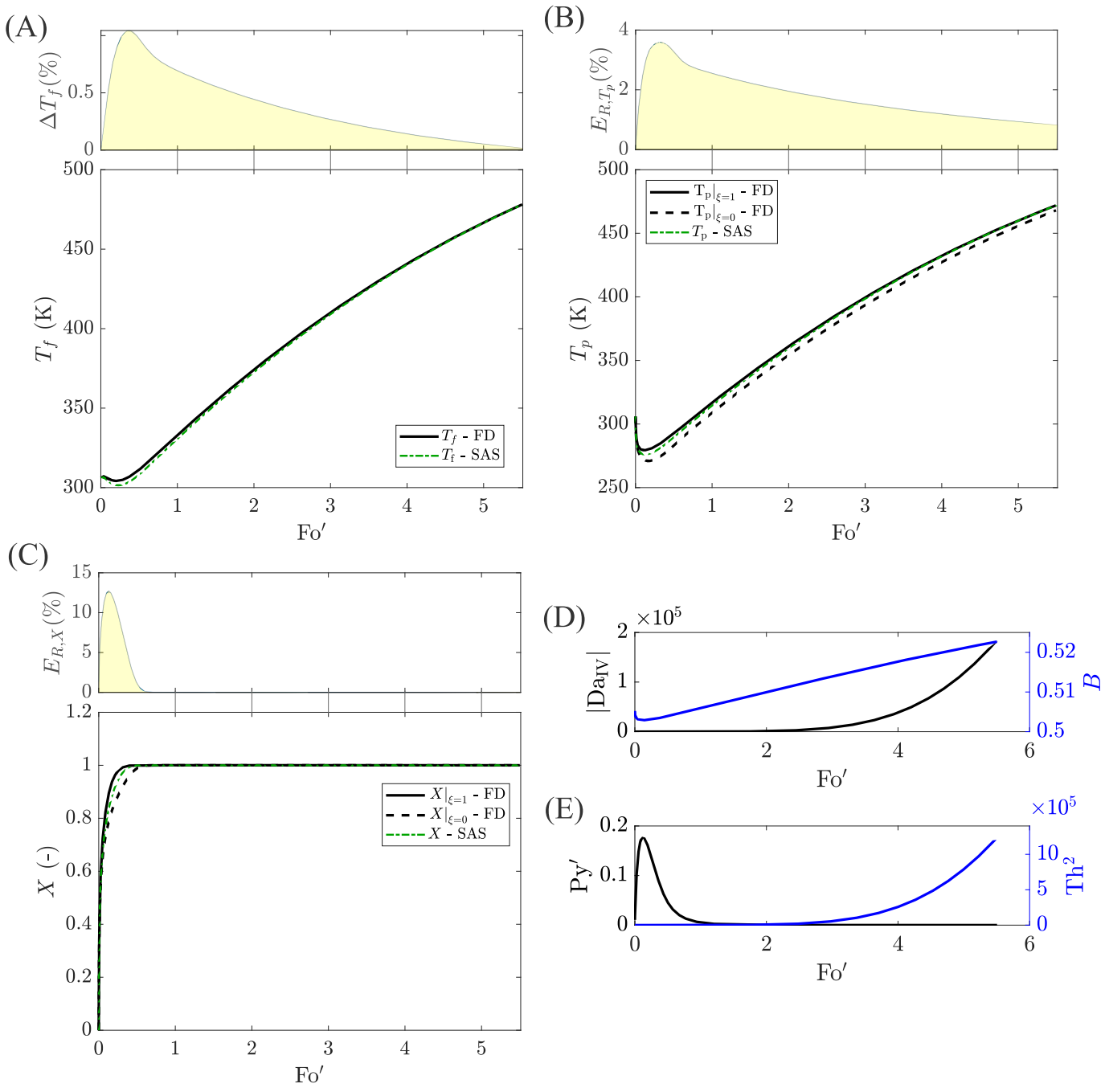

Figure 12

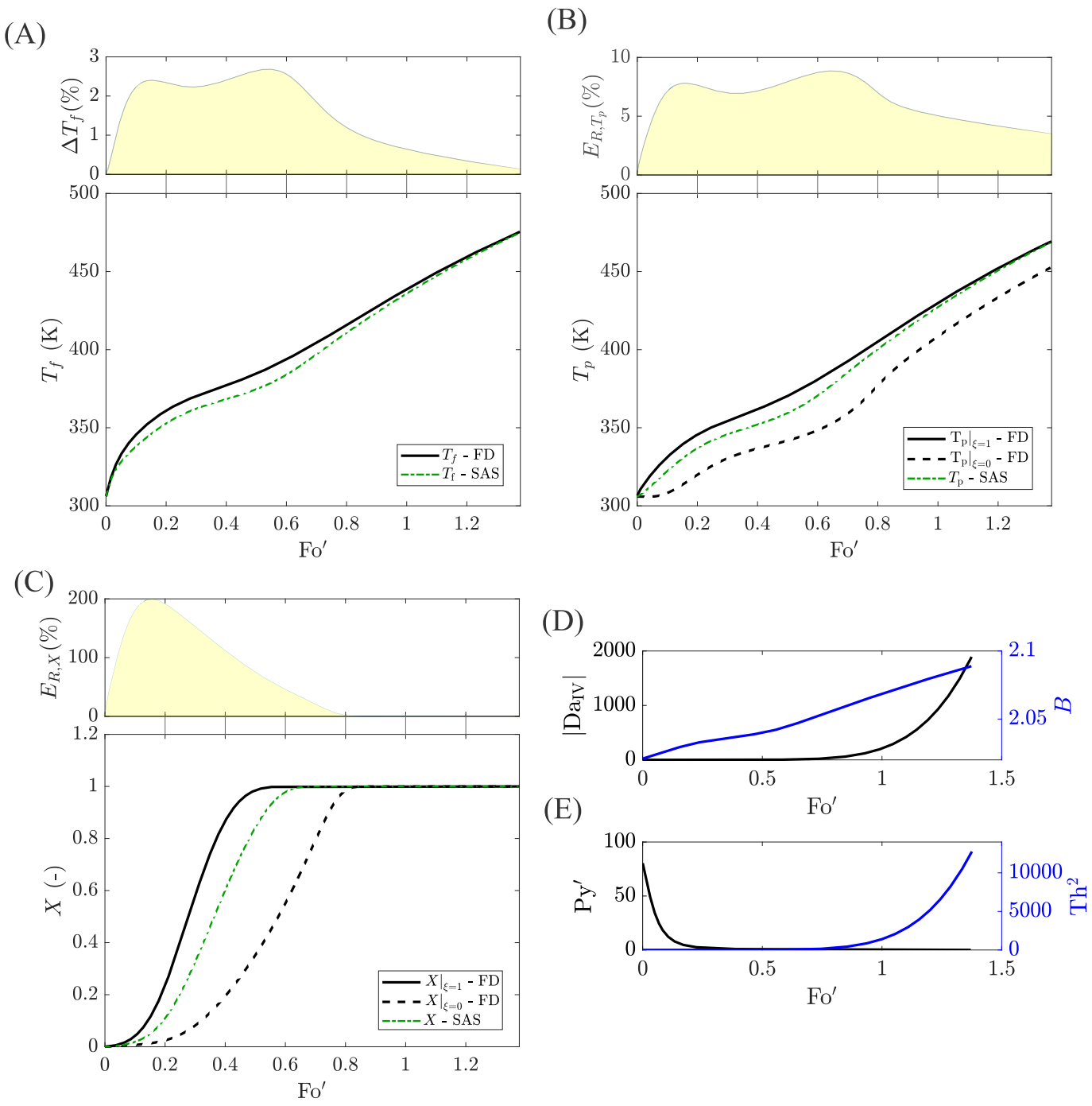

Figure 13